Journal of Computational Physics 386 (2019) 158–189

Contents lists available at ScienceDirect

Journal of Computational Physics

www.elsevier.com/locate/jcp

A simple diffuse interface approach on adaptive Cartesian grids for the linear elastic wave equations with complex topography

Maurizio Tavelli [a], Michael Dumbser [a,*], Dominic Etienne Charrier [b], Leonhard Rannabauer [c], Tobias Weinzierl [b], Michael Bader [c]

[a] Department of Civil, Environmental and Mechanical Engineering, University of Trento, Via Mesiano 77, I-38123 Trento, Italy
[b] Department of Computer Science, University of Durham, Lower Mountjoy, South Road, Durham DH1 3LE, United Kingdom
[c] Department of Informatics, Technical University Munich (TUM), Boltzmannstr. 3, D-85748 Garching, Germany

ARTICLE INFO

Article history:
Received 25 April 2018
Received in revised form 6 February 2019
Accepted 7 February 2019
Available online 18 February 2019

Keywords:
Diffuse interface method (DIM)
Complex geometries
High order schemes
Discontinuous Galerkin schemes
Adaptive mesh refinement (AMR)
Linear elasticity equations for seismic wave propagation

ABSTRACT

In most classical approaches of computational geophysics for seismic wave propagation problems, complex surface topography is either accounted for by boundary-fitted unstructured meshes, or, where possible, by mapping the complex computational domain from physical space to a topologically simple domain in a reference coordinate system. However, all these conventional approaches face problems if the geometry of the problem becomes sufficiently complex. They either need a mesh generator to create unstructured boundary-fitted grids, which can become quite difficult and may require a lot of manual user interactions in order to obtain a high quality mesh, or they need the explicit computation of an appropriate mapping function from physical to reference coordinates. For sufficiently complex geometries such mappings may either not exist or their Jacobian could become close to singular. Furthermore, in both conventional approaches low quality grids will always lead to very small time steps due to the Courant-Friedrichs-Lewy (CFL) condition for explicit schemes. In this paper, we propose a completely different strategy that follows the ideas of the successful family of high resolution shock-capturing schemes, where discontinuities can actually be resolved anywhere on the grid, without having to fit them exactly. We address the problem of geometrically complex free surface boundary conditions for seismic wave propagation problems with a novel diffuse interface method (DIM) on adaptive Cartesian meshes (AMR) that consists in the introduction of a characteristic function $0 \leq \alpha \leq 1$ which identifies the location of the solid medium and the surrounding air (or vacuum) and thus implicitly defines the location of the free surface boundary. Physically, α represents the volume fraction of the solid medium present in a control volume. Our new approach *completely avoids* the problem of mesh generation, since all that is needed for the definition of the complex surface topography is to set a scalar color function to unity inside the regions covered by the solid and to zero outside. The governing equations are derived from ideas typically used in the mathematical description of compressible multiphase flows. An analysis of the eigenvalues of the PDE system shows that the complexity of the geometry has no influence on the admissible time step size due to the CFL condition. The model reduces to the classical linear elasticity equations inside the solid medium where the gradients of α are zero, while in the diffuse interface zone at the free surface boundary the governing PDE system becomes nonlinear. We can prove that the solution of the Riemann problem with arbitrary data and a jump in α from

* Corresponding author.
E-mail addresses: m.tavelli@unitn.it (M. Tavelli), michael.dumbser@unitn.it (M. Dumbser), dominic.e.charrier@durham.ac.uk (D.E. Charrier), leo.rannabauer@tum.de (L. Rannabauer), tobias.weinzierl@durham.ac.uk (T. Weinzierl), bader@in.tum.de (M. Bader).

https://doi.org/10.1016/j.jcp.2019.02.004

unity to zero yields a Godunov-state at the interface that satisfies the free-surface boundary condition exactly, i.e. the normal stress components vanish. In the general case of an interface that is not aligned with the grid and which is not infinitely thin, a systematic study on the distribution of the volume fraction function inside the interface and the sensitivity with respect to the thickness of the diffuse interface layer has been carried out. In order to reduce numerical dissipation, we use high order discontinuous Galerkin (DG) finite element schemes on adaptive AMR grids together with a second order accurate high resolution shock capturing subcell finite volume (FV) limiter in the diffuse interface region. We furthermore employ a little dissipative HLLEM Riemann solver, which is able to resolve the steady contact discontinuity associated with the volume fraction function and the spatially variable material parameters exactly. While the method is locally high order accurate in the regions without limiter, the global order of accuracy of the scheme is at most two if the limiter is activated. It is locally of order one inside the diffuse interface region, which is typical for shock-capturing schemes at shocks and contact discontinuities. We show a large set of computational results in two and three space dimensions involving complex geometries where the physical interface is not aligned with the grid or where it is even moving. For all test cases we provide a quantitative comparison with classical approaches based on boundary-fitted unstructured meshes.

1. Introduction

The numerical solution of linear elastic wave propagation is still a challenging task, especially when complex three-dimensional geometries are involved. In the past, a large number of numerical schemes has been proposed for the simulation of seismic wave propagation. Madariaga [1] and Virieux [2,3] introduced finite difference schemes for the simulation of pressure (P) and shear (SV and SH) wave propagation. These schemes were then extended to higher order, see [4], three space dimensions [5,6] and to anisotropic material [7,8]. For finite difference-like methods on unstructured meshes we refer to the work of Magnier et al. [9] and Käser & Igel [10,11]. There are also several applications in the context of finite volume (FV) schemes [12–17], which, however, were all limited to second order of accuracy in space and time. The first arbitrary high order ADER finite volume scheme for seismic wave propagation was introduced in [18]. For real applications it is crucial that a numerical scheme is able to properly capture complex signals over long distances and times. In contrast to classical low order schemes, high order methods in space and time are able to better reproduce the time evolution of the solution. A quantitative accuracy analysis of high order numerical schemes for linear elasticity, based on the misfit criteria developed in [19,20], can be found in [21,22]. Spectral finite element methods [23] were successfully applied to linear elastic wave propagation in a well-known series of paper of Komatitsch and collaborators [24–28]. For Chebyshev spectral methods for wave propagation we refer to the work of Tessmer et al. [29,8] and Igel [30]. For alternative developments in the framework of stabilized continuous finite elements applied to elastic and acoustic wave propagation we refer to [31–33]. Apart from wave propagation in the medium, also the proper representation of complex surface topography is a challenging task. For this purpose, several high order numerical schemes on unstructured meshes were introduced in the past. A series of explicit high order discontinuous Galerkin (DG) schemes for elastic wave propagation on unstructured meshes was proposed in [34–39], while the concept of space-time discontinuous Galerkin schemes, originally introduced and analyzed in [40–46] for computational fluid dynamics (CFD), was later also extended to linear elasticity in [47–49]. The space-time DG method used in [49] is based on the novel concept of *staggered* discontinuous Galerkin finite element schemes, which was introduced for CFD problems in [50–56]. In any case, all previous methods require a boundary-fitted mesh that properly represents the geometry of the physical problem to be solved. The generation of this mesh is in general a highly non-trivial task and usually requires the use of external mesh generation tools. Moreover, the mesh generation process in highly complex geometry can lead to very small elements with bad aspect ratio, so-called *sliver elements* [57–59]. This well known problem can often be avoided, but not always, see e.g. [60,61]. For explicit time discretization, sliver elements can only be treated at the aid of *local time stepping* (LTS), see, for example, [36,62–64], but currently only very few schemes used in production codes employed in computational seismology support time-accurate local time stepping. Alternatively, implicit schemes like [49] require the introduction of a proper preconditioner in order to limit the number of iterations needed to solve the associated linear algebraic system.

The *key idea* of this paper is therefore to *completely avoid* the mesh generation problem associated with classical approaches used in computational seismology. This is achieved by extending the linear elastic wave equations via a characteristic (color) function α, which is nothing else than the volume fraction of the solid medium, and which determines if a point $\mathbf{x}$ is located inside the solid material ($\alpha(\mathbf{x}) = 1$) or outside ($\alpha(\mathbf{x}) = 0$). In this way the scalar parameter α simply determines the physical boundary through a diffuse interface zone, instead of requiring a boundary-fitted structured or unstructured mesh. With this new approach, even very complex geometries can be easily represented on regular adaptive Cartesian meshes, i.e. via the use of adaptive mesh refinement (AMR). Furthermore, the introduction of the new parameter α does not change the eigenvalues of the PDE system and therefore does not influence the time step restriction imposed by

the CFL condition. To be more precise: the admissible time step size of the new approach presented in this paper depends of course on the chosen *mesh spacing* of the regular AMR grid and on the *signal speeds* in the PDE system, but it does *not* explicitly depend on the *mesh quality* and the *geometric complexity* of the computational domain, as it is the case for many other approaches in computational seismology.

In the context of finite difference schemes for seismic wave propagation, immersed boundary methods for the treatment of complex free surface topologies can be found, for example, in [65–68] and references therein. However, the underlying mathematical models used there are *different* from the one proposed in this paper, which is based on a diffuse interface approach that is used for the description of compressible multi-phase flows in computational fluid dynamics.

Our new method is inspired by the work concerning the modeling and simulation of compressible multiphase flows, see [69] and [70–73]. It can also be interpreted as a special case of the more general symmetric hyperbolic and thermodynamically compatible model of nonlinear hyperelasticity of Godunov & Romenski and collaborators [74–80]. A diffuse interface approach, similar to the one used in this paper, has already been successfully applied to nonlinear compressible fluid-structure interaction problems in a series of papers [81–83], but the employed numerical methods were only low order accurate in space and time and therefore not suitable for seismic wave propagation problems. Other applications of diffuse interface methods for compressible multi-phase flows can be found in [84–86], but, to the best of our knowledge, this is the first time that a diffuse interface approach is derived and validated for linear seismic wave propagation in complex geometries. Within the present paper, we use high order accurate ADER-DG schemes on Cartesian meshes with adaptive mesh refinement (AMR). The numerical method has already successfully been applied to other hyperbolic PDE systems [87,78]. The use of adaptive mesh refinement allows to increase the resolution locally where needed, especially close to the free surface or at internal material boundaries. To avoid spurious oscillations and to enforce nonlinear stability, we use a simple but very robust *a posteriori* subcell finite volume (FV) limiter [88]. Here, a *second order* total variation diminishing (TVD) finite volume scheme is adopted in the limited DG cells. In order to maintain accuracy, the subgrid of the limiter is by a factor of $2N+1$ times finer compared to the grid of an unlimited DG scheme with polynomial approximation degree N. The idea of using an *a posteriori* approach to limit high order schemes was first proposed by Clain, Diot and Loubère within the so-called Multi-dimensional Optimal Order Detection (MOOD) paradigm in the context of finite volume schemes, see [89,90] for more details. Finally, in our numerical scheme we make use of the HLLEM Riemann solver introduced in [91,92], which is able to resolve the steady contact discontinuities associated with the spatially variable material parameters λ and μ (the Lamé constants), the mass density ρ and the volume fraction α. The numerical results presented later in this paper show that the proposed methodology seems to be a valid alternative to existing approaches in computational seismology that are based on boundary-fitted structured or unstructured meshes. At this point we would like to stress that the use of a second order shock capturing TVD finite volume scheme inside the diffuse interface region at the free surface boundary limits the *global* order of accuracy of the scheme to at most two. Numerical experiments further show that the method is locally first order accurate inside the diffuse interface region, which is well-known from shock capturing finite volume schemes in CFD, which also reduce to first order of accuracy at shocks and contact discontinuities that are not exactly resolved on the grid, see [93]. Nevertheless, the *unlimited* ADER-DG scheme that is used inside the solid medium and far from the free surface boundary is *locally* high order accurate and thus beneficial concerning phase and amplitude errors for wave propagation over long distances and times *inside* the solid medium. Note that the manifold describing the free surface is of one dimension less than the computational domain, hence most cells can actually use the high order accurate *unlimited* DG scheme and only very few cells require the use of the second order accurate subcell finite volume limiter. In order to reduce the numerical errors in the diffuse interface region as far as possible, we propose to use adaptive mesh refinement (AMR) with time-accurate local time stepping (LTS) combined with a subcell FV limiter, where the subgrid is by a factor of $2N+1$ times finer than the grid of the unlimited ADER-DG scheme with polynomial approximation degree N. However, we would like to emphasize that the mathematical model proposed in this paper is *not* strictly linked to the numerical schemes that are used in this paper for its solution (ADER-DG with AMR coupled with subcell finite volume limiter). Any standard finite difference scheme inside the solid together with a nonlinear ENO/WENO scheme at the free surface where $\nabla\alpha \neq 0$ could have been applied equally well.

The rest of the paper is organized as follows: in Section 2 we introduce the governing PDE of the new diffuse interface approach for linear elasticity. We also show the compatibility of our model with the free surface boundary condition in the case where α jumps from 1 to 0. In Section 3 we briefly summarize the high order ADER-DG schemes used in this paper. In Section 4 we show numerical results for a large set of test problems in two and three space dimensions, also including a realistic 3D scenario with complex geometry given by real DTM data. Finally, in Section 5 we give some concluding remarks and an outlook on future work, which will concern nonlinear large-strain elasto-plasticity and dynamic rupture processes in moving media based on the theory of nonlinear hyperelasticity of Godunov and Romenski [74,94,77].

2. Mathematical model

The equations of linear elasticity [95] can be written as

$$\frac{\partial}{\partial t}\sigma_{xx} - (\lambda+2\mu)\frac{\partial}{\partial x}u - \lambda\frac{\partial}{\partial y}v - \lambda\frac{\partial}{\partial z}w = S_{xx},$$

$$
\begin{aligned}
\frac{\partial}{\partial t}\sigma_{yy} - \lambda\frac{\partial}{\partial x}u - (\lambda+2\mu)\frac{\partial}{\partial y}v - \lambda\frac{\partial}{\partial z}w &= S_{yy},\\
\frac{\partial}{\partial t}\sigma_{zz} - \lambda\frac{\partial}{\partial x}u - \lambda\frac{\partial}{\partial y}v - (\lambda+2\mu)\frac{\partial}{\partial z}w &= S_{zz},\\
\frac{\partial}{\partial t}\sigma_{xy} - \mu\left(\frac{\partial}{\partial x}v + \frac{\partial}{\partial y}u\right) &= S_{xy},\\
\frac{\partial}{\partial t}\sigma_{yz} - \mu\left(\frac{\partial}{\partial z}v + \frac{\partial}{\partial y}w\right) &= S_{yz},\\
\frac{\partial}{\partial t}\sigma_{xz} - \mu\left(\frac{\partial}{\partial z}u + \frac{\partial}{\partial x}w\right) &= S_{xz},\\
\frac{\partial}{\partial t}(\rho u) - \frac{\partial}{\partial x}\sigma_{xx} - \frac{\partial}{\partial y}\sigma_{xy} - \frac{\partial}{\partial z}\sigma_{xz} &= \rho S_u,\\
\frac{\partial}{\partial t}(\rho v) - \frac{\partial}{\partial x}\sigma_{xy} - \frac{\partial}{\partial y}\sigma_{yy} - \frac{\partial}{\partial z}\sigma_{yz} &= \rho S_v,\\
\frac{\partial}{\partial t}(\rho w) - \frac{\partial}{\partial x}\sigma_{xz} - \frac{\partial}{\partial y}\sigma_{yz} - \frac{\partial}{\partial z}\sigma_{zz} &= \rho S_w,
\end{aligned}
\tag{1}
$$

where λ and μ are the so called Lamé constants and ρ is the mass density. In more compact form the above system reads

$$
\frac{\partial \boldsymbol{\sigma}}{\partial t} - \mathbf{E}(\lambda,\mu)\cdot\nabla\boldsymbol{v} = \boldsymbol{S}_\sigma, \tag{2}
$$

$$
\frac{\partial \rho\boldsymbol{v}}{\partial t} - \nabla\cdot\boldsymbol{\sigma} = \rho\boldsymbol{S}_v, \tag{3}
$$

where $\boldsymbol{v} = (u, v, w)$ is the velocity field, ρ is the material density, $\boldsymbol{S}_\rho$ and $\boldsymbol{S}_\sigma$ are volume or point sources, $\boldsymbol{\sigma}$ is the symmetric stress tensor, and $\mathbf{E}(\lambda,\mu)$ is the stiffness tensor that connects the strain tensor ϵ_{kl} to the stress tensor $\boldsymbol{\sigma}$ according to the Hooke law $\boldsymbol{\sigma} = \mathbf{E}\boldsymbol{\epsilon}$. The stress tensor $\boldsymbol{\sigma}$ is given by

$$
\boldsymbol{\sigma} = \begin{pmatrix} \sigma_{xx} & \sigma_{xy} & \sigma_{xz} \\ \sigma_{yx} & \sigma_{yy} & \sigma_{yz} \\ \sigma_{zx} & \sigma_{zy} & \sigma_{zz} \end{pmatrix} \tag{4}
$$

with the symmetry $\sigma_{ij} = \sigma_{ji}$. The normal stress components are σ_{xx}, σ_{yy} and σ_{zz}, while the shear stress is represented by σ_{xy}, σ_{yz} and σ_{xz}. The stress tensor $\boldsymbol{\sigma}$ can thus be written in terms of its six independent components $(\sigma_{xx}, \sigma_{yy}, \sigma_{zz}, \sigma_{xy}, \sigma_{yz}, \sigma_{xz})$. In the following we propose a new model that follows the ideas used in the simulation of compressible multiphase flows [69–71,73]. In order to derive the model we start from a Baer-Nunziato-type system for the description of compressible multi-phase flows, where for the solid phase (index s) the pressure term has been appropriately replaced by the stress tensor $\boldsymbol{\sigma}_s$, and where the usual pressure and velocity relaxation source terms have been dropped:

$$
\begin{aligned}
\frac{\partial}{\partial t}(\alpha_s\rho_s) + \nabla\cdot(\alpha_s\rho_s\mathbf{v}_s) &= 0,\\
\frac{\partial}{\partial t}(\alpha_s\rho_s\mathbf{v}_s) + \nabla\cdot(\alpha_s\rho_s\mathbf{v}_s\otimes\mathbf{v}_s + \alpha_s\boldsymbol{\sigma}_s) - \boldsymbol{\sigma}_I\nabla\alpha_s &= \alpha_s\rho_s\mathbf{S}_{v,s},\\
\frac{\partial}{\partial t}(\alpha_s\rho_s E_s) + \nabla\cdot(\alpha_s\rho_s E_s\mathbf{v}_s + \alpha_s\boldsymbol{\sigma}_s\mathbf{v}_s) - \boldsymbol{\sigma}_I\nabla\alpha_s\cdot\mathbf{v}_I &= \alpha_s\rho_s\mathbf{S}_{v,s}\cdot\mathbf{v}_s,\\
\frac{\partial}{\partial t}\left(\alpha_g\rho_g\right) + \nabla\cdot\left(\alpha_g\rho_g\mathbf{v}_g\right) &= 0,\\
\frac{\partial}{\partial t}\left(\alpha_g\rho_g\mathbf{v}_g\right) + \nabla\cdot\left(\alpha_g\rho_g\mathbf{v}_g\otimes\mathbf{v}_g + \alpha_g\boldsymbol{\sigma}_g\right) - \boldsymbol{\sigma}_g\nabla\alpha_g &= \alpha_g\rho_g\mathbf{S}_{v,g},\\
\frac{\partial}{\partial t}\left(\alpha_g\rho_g E_g\right) + \nabla\cdot\left(\alpha_g\rho_g E_g\mathbf{v}_g + \alpha_g\boldsymbol{\sigma}_g\mathbf{v}_g\right) - \boldsymbol{\sigma}_I\nabla\alpha_g\cdot\mathbf{v}_I &= \alpha_g\rho_g\mathbf{S}_{v,g}\cdot\mathbf{v}_g,\\
\frac{\partial}{\partial t}\alpha_s + \mathbf{v}_I\nabla\alpha_s &= 0.
\end{aligned}
\tag{5}
$$

Here index s refers to the solid phase and index g refers to the gas phase surrounding the solid; ρ_k is the mass density and E_k is the specific total energy of phase k, $\mathbf{v}_k$ is the phase velocity, $\mathbf{v}_I$ is the so-called interface velocity and $\boldsymbol{\sigma}_I$ is the stress tensor at the interface, which is a generalization of the interface pressure used in standard BN models. We now make the following simplifying assumptions:

(i) The interface between the solid and the gas is moving only at a negligible speed, hence we can assume $\mathbf{v}_I = 0$.
(ii) Compared to the original Baer-Nunziato model [69,96,86], all pressure and velocity *relaxation source terms* are *neglected*.
(iii) The mass density of the gas phase is much smaller than the one of the solid phase ($\rho_g \ll \rho_s$), hence the time evolution of the gas phase is not relevant for our purposes. Therefore, all evolution equations related to the gas phase can be neglected in the following, similar to the approach used in [97–99] in the context of non-hydrostatic free surface flow simulations based on a diffuse interface approach. To ease notation, the remaining index s for the solid phase can be dropped.
(iv) We assume the density ρ_s of the solid phase to be constant in time, so the related mass conservation equation can be neglected.
(v) The stress tensor of the solid can be directly calculated via Hooke's law (2), so it is not necessary to evolve the total energy conservation law for the solid.
(vi) The nonlinear convective term $\alpha_s \rho_s \mathbf{v}_s \otimes \mathbf{v}_s$, which is quadratic in the solid velocity, can be neglected, since the solid velocity is assumed to be small in the linear elasticity limit.
(vii) Last but not least, the free surface boundary condition at the interface between solid and surrounding gas leads to $\boldsymbol{\sigma}_I \cdot \nabla \alpha_s = 0$.

As a result of these simplifying assumptions, the *reduced* governing PDE system of the new diffuse interface approach for linear elasticity in complex geometry reads:

$$\frac{\partial \boldsymbol{\sigma}}{\partial t} - \mathbf{E}(\lambda, \mu) \cdot \nabla \boldsymbol{v} = \boldsymbol{S}_\sigma, \tag{6}$$

$$\frac{\partial \alpha \rho \boldsymbol{v}}{\partial t} - \nabla \cdot (\alpha \boldsymbol{\sigma}) = \alpha \rho \boldsymbol{S}_v, \tag{7}$$

$$\frac{\partial \alpha}{\partial t} = 0. \tag{8}$$

Since $\partial_t \rho = 0$, the previous equations are then rewritten as

$$\frac{\partial \boldsymbol{\sigma}}{\partial t} - \mathbf{E}(\lambda, \mu) \cdot \frac{1}{\alpha} \nabla (\alpha \boldsymbol{v}) + \frac{1}{\alpha} \mathbf{E}(\lambda, \mu) \cdot \boldsymbol{v} \otimes \nabla \alpha = \boldsymbol{S}_\sigma, \tag{9}$$

$$\frac{\partial \alpha \boldsymbol{v}}{\partial t} - \frac{\alpha}{\rho} \nabla \cdot \boldsymbol{\sigma} - \frac{1}{\rho} \boldsymbol{\sigma} \cdot \nabla \alpha = \boldsymbol{S}_v, \tag{10}$$

$$\frac{\partial \alpha}{\partial t} = 0. \tag{11}$$

Furthermore the following equations for the material parameters are added to the system:

$$\frac{\partial \lambda}{\partial t} = 0, \qquad \frac{\partial \mu}{\partial t} = 0, \qquad \frac{\partial \rho}{\partial t} = 0. \tag{12}$$

The material parameters λ, μ and ρ are assumed to be constant in time but *not* in space, i.e. $\lambda = \lambda(\mathbf{x}), \mu = \mu(\mathbf{x})$ and $\rho = \rho(\mathbf{x})$, for which we will use a high order polynomial representation as for the other variables of the PDE system. The same diffuse interface model (6)-(8) can also be obtained by combining the nonlinear hyperelasticity equations of Godunov and Romenski [74,94,100] with the compressible multi-phase model of Romenski et al. [75,101], assuming linear material behavior and neglecting nonlinear convective terms. System (9)-(12) is then rewritten in the following form:

$$\frac{\partial \mathbf{Q}}{\partial t} + \mathbf{B}_1(\mathbf{Q}) \frac{\partial \mathbf{Q}}{\partial x} + \mathbf{B}_2(\mathbf{Q}) \frac{\partial \mathbf{Q}}{\partial y} + \mathbf{B}_3(\mathbf{Q}) \frac{\partial \mathbf{Q}}{\partial z} = \boldsymbol{S}(\mathbf{x}, t), \tag{13}$$

where the three matrices $\mathbf{B}_1$, $\mathbf{B}_2$ and $\mathbf{B}_3$ are specified in Eqs. (15)-(17). The vector $\mathbf{Q}$ is given by

$$\mathbf{Q} = \left(\sigma_{xx}, \sigma_{yy}, \sigma_{zz}, \sigma_{xy}, \sigma_{yz}, \sigma_{xz}, \alpha u, \alpha v, \alpha w, \lambda, \mu, \rho, \alpha\right)^\top, \tag{14}$$

while the matrices $\mathbf{B}_1$, $\mathbf{B}_2$ and $\mathbf{B}_3$ read

$$\mathbf{B}_1 = \begin{pmatrix}
0 & 0 & 0 & 0 & 0 & 0 & -\frac{1}{\alpha}(\lambda+2\mu) & 0 & 0 & 0 & 0 & 0 & \frac{1}{\alpha}(\lambda+2\mu)u \\
0 & 0 & 0 & 0 & 0 & 0 & -\frac{1}{\alpha}\lambda & 0 & 0 & 0 & 0 & 0 & \frac{1}{\alpha}\lambda u \\
0 & 0 & 0 & 0 & 0 & 0 & -\frac{1}{\alpha}\lambda & 0 & 0 & 0 & 0 & 0 & \frac{1}{\alpha}\lambda u \\
0 & 0 & 0 & 0 & 0 & 0 & 0 & -\frac{1}{\alpha}\mu & 0 & 0 & 0 & 0 & \frac{1}{\alpha}\mu v \\
0 & 0 & 0 & 0 & 0 & 0 & 0 & 0 & 0 & 0 & 0 & 0 & 0 \\
0 & 0 & 0 & 0 & 0 & 0 & 0 & 0 & -\frac{1}{\alpha}\mu & 0 & 0 & 0 & \frac{1}{\alpha}\mu w \\
-\frac{\alpha}{\rho} & 0 & 0 & 0 & 0 & 0 & 0 & 0 & 0 & 0 & 0 & 0 & -\frac{1}{\rho}\sigma_{xx} \\
0 & 0 & 0 & -\frac{\alpha}{\rho} & 0 & 0 & 0 & 0 & 0 & 0 & 0 & 0 & -\frac{1}{\rho}\sigma_{xy} \\
0 & 0 & 0 & 0 & 0 & -\frac{\alpha}{\rho} & 0 & 0 & 0 & 0 & 0 & 0 & -\frac{1}{\rho}\sigma_{xz} \\
0 & 0 & 0 & 0 & 0 & 0 & 0 & 0 & 0 & 0 & 0 & 0 & 0 \\
0 & 0 & 0 & 0 & 0 & 0 & 0 & 0 & 0 & 0 & 0 & 0 & 0 \\
0 & 0 & 0 & 0 & 0 & 0 & 0 & 0 & 0 & 0 & 0 & 0 & 0 \\
0 & 0 & 0 & 0 & 0 & 0 & 0 & 0 & 0 & 0 & 0 & 0 & 0
\end{pmatrix}, \tag{15}$$

$$\mathbf{B}_2 = \begin{pmatrix}
0 & 0 & 0 & 0 & 0 & 0 & 0 & -\frac{1}{\alpha}\lambda & 0 & 0 & 0 & 0 & \frac{1}{\alpha}\lambda v \\
0 & 0 & 0 & 0 & 0 & 0 & 0 & -\frac{1}{\alpha}(\lambda+2\mu) & 0 & 0 & 0 & 0 & \frac{1}{\alpha}(\lambda+2\mu)v \\
0 & 0 & 0 & 0 & 0 & 0 & 0 & -\frac{1}{\alpha}\lambda & 0 & 0 & 0 & 0 & \frac{1}{\alpha}\lambda v \\
0 & 0 & 0 & 0 & 0 & 0 & -\frac{1}{\alpha}\mu & 0 & 0 & 0 & 0 & 0 & \frac{1}{\alpha}\mu u \\
0 & 0 & 0 & 0 & 0 & 0 & 0 & 0 & -\frac{1}{\alpha}\mu & 0 & 0 & 0 & \frac{1}{\alpha}\mu w \\
0 & 0 & 0 & 0 & 0 & 0 & 0 & 0 & 0 & 0 & 0 & 0 & 0 \\
0 & 0 & 0 & -\frac{\alpha}{\rho} & 0 & 0 & 0 & 0 & 0 & 0 & 0 & 0 & -\frac{1}{\rho}\sigma_{xy} \\
0 & -\frac{\alpha}{\rho} & 0 & 0 & 0 & 0 & 0 & 0 & 0 & 0 & 0 & 0 & -\frac{1}{\rho}\sigma_{yy} \\
0 & 0 & 0 & 0 & -\frac{\alpha}{\rho} & 0 & 0 & 0 & 0 & 0 & 0 & 0 & -\frac{1}{\rho}\sigma_{yz} \\
0 & 0 & 0 & 0 & 0 & 0 & 0 & 0 & 0 & 0 & 0 & 0 & 0 \\
0 & 0 & 0 & 0 & 0 & 0 & 0 & 0 & 0 & 0 & 0 & 0 & 0 \\
0 & 0 & 0 & 0 & 0 & 0 & 0 & 0 & 0 & 0 & 0 & 0 & 0 \\
0 & 0 & 0 & 0 & 0 & 0 & 0 & 0 & 0 & 0 & 0 & 0 & 0
\end{pmatrix}, \tag{16}$$

$$\mathbf{B}_3 = \begin{pmatrix}
0 & 0 & 0 & 0 & 0 & 0 & 0 & 0 & -\frac{1}{\alpha}\lambda & 0 & 0 & 0 & \frac{1}{\alpha}\lambda w \\
0 & 0 & 0 & 0 & 0 & 0 & 0 & 0 & -\frac{1}{\alpha}\lambda & 0 & 0 & 0 & \frac{1}{\alpha}\lambda w \\
0 & 0 & 0 & 0 & 0 & 0 & 0 & 0 & -\frac{1}{\alpha}(\lambda+2\mu) & 0 & 0 & 0 & \frac{1}{\alpha}(\lambda+2\mu)w \\
0 & 0 & 0 & 0 & 0 & 0 & 0 & 0 & 0 & 0 & 0 & 0 & 0 \\
0 & 0 & 0 & 0 & 0 & 0 & 0 & -\frac{1}{\alpha}\mu & 0 & 0 & 0 & 0 & \frac{1}{\alpha}\mu v \\
0 & 0 & 0 & 0 & 0 & 0 & -\frac{1}{\alpha}\mu & 0 & 0 & 0 & 0 & 0 & \frac{1}{\alpha}\mu u \\
0 & 0 & 0 & 0 & 0 & -\frac{\alpha}{\rho} & 0 & 0 & 0 & 0 & 0 & 0 & -\frac{1}{\rho}\sigma_{xz} \\
0 & 0 & 0 & 0 & -\frac{\alpha}{\rho} & 0 & 0 & 0 & 0 & 0 & 0 & 0 & -\frac{1}{\rho}\sigma_{yz} \\
0 & 0 & -\frac{\alpha}{\rho} & 0 & 0 & 0 & 0 & 0 & 0 & 0 & 0 & 0 & -\frac{1}{\rho}\sigma_{zz} \\
0 & 0 & 0 & 0 & 0 & 0 & 0 & 0 & 0 & 0 & 0 & 0 & 0 \\
0 & 0 & 0 & 0 & 0 & 0 & 0 & 0 & 0 & 0 & 0 & 0 & 0 \\
0 & 0 & 0 & 0 & 0 & 0 & 0 & 0 & 0 & 0 & 0 & 0 & 0 \\
0 & 0 & 0 & 0 & 0 & 0 & 0 & 0 & 0 & 0 & 0 & 0 & 0
\end{pmatrix}. \tag{17}$$

The eigenvalues associated with the matrix $\mathbf{B}_1$ are

$$\lambda_1 = -c_p, \quad \lambda_{2,3} = -c_s, \quad \lambda_{4,5,6,7,8,9,10} = 0, \quad \lambda_{11,12} = +c_s, \quad \lambda_{13} = +c_p, \tag{18}$$

where

$$c_p = \sqrt{\frac{\lambda+2\mu}{\rho}} \qquad \text{and} \qquad c_s = \sqrt{\frac{\mu}{\rho}} \tag{19}$$

are the $p-$ and $s-$ wave velocities, respectively. The matrix of right eigenvectors of the matrix $\mathbf{B}_1$ as defined in (15) is given by

$$\mathbf{R} = \begin{pmatrix}
\rho c_p^2 & 0 & 0 & 0 & 0 & 0 & 0 & 0 & 0 & -\sigma_{xx} & 0 & 0 & \rho c_p^2 \\
\rho(c_p^2 - 2c_s^2) & 0 & 0 & 1 & 0 & 0 & 0 & 0 & 0 & 0 & 0 & 0 & \rho(c_p^2 - 2c_s^2) \\
\rho(c_p^2 - 2c_s^2) & 0 & 0 & 0 & 1 & 0 & 0 & 0 & 0 & 0 & 0 & 0 & \rho(c_p^2 - 2c_s^2) \\
0 & \rho c_s^2 & 0 & 0 & 0 & 0 & 0 & 0 & 0 & -\sigma_{xy} & 0 & \rho c_s^2 & 0 \\
0 & 0 & 0 & 0 & 0 & 1 & 0 & 0 & 0 & 0 & 0 & 0 & 0 \\
0 & 0 & \rho c_s^2 & 0 & 0 & 0 & 0 & 0 & 0 & -\sigma_{xz} & \rho c_s^2 & 0 & 0 \\
c_p & 0 & 0 & 0 & 0 & 0 & 0 & 0 & 0 & \alpha u & 0 & 0 & -c_p \\
0 & c_s & 0 & 0 & 0 & 0 & 0 & 0 & 0 & \alpha v & 0 & -c_s & 0 \\
0 & 0 & c_s & 0 & 0 & 0 & 0 & 0 & 0 & \alpha w & -c_s & 0 & 0 \\
0 & 0 & 0 & 0 & 0 & 0 & 0 & 0 & 1 & 0 & 0 & 0 & 0 \\
0 & 0 & 0 & 0 & 0 & 0 & 0 & 1 & 0 & 0 & 0 & 0 & 0 \\
0 & 0 & 0 & 0 & 0 & 0 & 1 & 0 & 0 & 0 & 0 & 0 & 0 \\
0 & 0 & 0 & 0 & 0 & 0 & 0 & 0 & 0 & \alpha & 0 & 0 & 0
\end{pmatrix}. \tag{20}$$

The expressions for the eigenvalues and eigenvectors of $\mathbf{B}_2$ and $\mathbf{B}_3$ are very similar and can be obtained from those of $\mathbf{B}_1$, since the PDE system is rotationally invariant. For this reason, we do not give their explicit expressions here. We now want to show that the proposed model satisfies the free surface boundary condition $\boldsymbol{\sigma} \cdot \mathbf{n} = 0$ exactly when considering a Riemann problem that includes a jump of α from $\alpha^L = 1$ to $\alpha^R = 0$.

For this, consider the left and right state of a Riemann problem in the x-direction given by

$$\mathbf{Q}_L = (\sigma_{xx}^L, \sigma_{yy}^L, \sigma_{zz}^L, \sigma_{xy}^L, \sigma_{yz}^L, \sigma_{xz}^L, u^L, v^L, w^L, \lambda, \mu, \rho, 1), \tag{21}$$

$$\mathbf{Q}_R = (\sigma_{xx}^R, \sigma_{yy}^R, \sigma_{zz}^R, \sigma_{xy}^R, \sigma_{yz}^R, \sigma_{xz}^R, 0, 0, 0, \lambda, \mu, \rho, 0). \tag{22}$$

By using a simple straight line segment path

$$\psi(s) = \mathbf{Q}_L + s\,(\mathbf{Q}_R - \mathbf{Q}_L)\,, \tag{23}$$

we can define a generalized Roe-averaged matrix $\tilde{\mathbf{B}}_1$ in x direction according to [102–104] as follows:

$$\tilde{\mathbf{B}}_1 = \int_0^1 \mathbf{B}_1(\psi(s))ds. \tag{24}$$

The exact solution of the linearized Riemann problem based on the Roe-averaged matrix $\tilde{\mathbf{B}}_1 = \tilde{\mathbf{R}}\tilde{\boldsymbol{\Lambda}}\tilde{\mathbf{R}}^{-1}$ above and the similarity coordinate $\xi = x/t$ reads

$$\mathbf{Q}_{\mathrm{RP}}(\xi) = \frac{1}{2}\tilde{\mathbf{R}}\left(\mathbf{I} - \mathrm{sign}(\xi\mathbf{I} - \tilde{\boldsymbol{\Lambda}})\right)\tilde{\mathbf{R}}^{-1} \cdot \mathbf{Q}_L + \frac{1}{2}\tilde{\mathbf{R}}\left(\mathbf{I} + \mathrm{sign}(\xi\mathbf{I} - \tilde{\boldsymbol{\Lambda}})\right)\tilde{\mathbf{R}}^{-1} \cdot \mathbf{Q}_R, \tag{25}$$

with $\mathbf{I}$ being the identity matrix. From $\mathbf{Q}_{\mathrm{RP}}(\xi)$ we can obtain the following *Godunov state* $\mathbf{Q}_{\mathrm{God}} = \mathbf{Q}_{\mathrm{RP}}(0)$ at the interface $(\xi = 0)$

$$\mathbf{Q}_{\mathrm{God}} = \left(0, \frac{\sigma_{xx}^L c_p^2 + 2\sigma_{xx}^L c_s^2 + \sigma_{yy} c_p^2}{c_p^2}, \frac{\sigma_{xx}^L c_p^2 + 2\sigma_{xx}^L c_s^2 + \sigma_{zz} c_p^2}{c_p^2}, 0, \sigma_{yz}^L, 0, \right.$$
$$\left. \frac{c_p \rho u^L - \sigma_{xx}^L}{c_p \rho}, \frac{c_s \rho v^L - \sigma_{xy}^L}{c_s \rho}, \frac{c_s \rho w^L - \sigma_{xz}^L}{c_s \rho}, \lambda, \mu, \rho, 1\right),$$

from which it is clear that all the components of the normal stress in x-direction (σ_{xx}, σ_{xy} and σ_{xz}) are zero, which means that the free surface boundary condition $\boldsymbol{\sigma} \cdot \mathbf{n} = 0$ is indeed respected by merely imposing a jump in the volume fraction function from $\alpha = 1$ to $\alpha = 0$.

As one can note, the model (9)-(11) involves divisions by α that can be a source of instabilities at the interface, since the color function α is ideally set to zero, or at least close to zero, outside the solid medium. In order to address this problem, we introduce a simple transformation that avoids the divisions by zeros. In particular, we substitute all multiplications by $\alpha^{-1} = 1/\alpha$, with

$$\alpha^{-1} \cong \frac{\alpha}{\alpha^2 + \epsilon(\alpha)}, \tag{26}$$

where $\epsilon = \epsilon(\alpha)$ has to satisfy $\epsilon(1) = 0$ and $\epsilon(0) = \epsilon_0 > 0$ in order to be consistent with the linear elasticity equations. In our case we take a simple linear function $\epsilon = \epsilon_0(1 - \alpha)$ with $\epsilon_0 = 10^{-3}$. The introduction of this new parameter with this method is mandatory to obtain a stable solution. The new eigenvalues are $\tilde{\lambda} = f\lambda$, where $f = \frac{\alpha}{\sqrt{\alpha^2 + \epsilon_0(1-\alpha)}}$ that for $\alpha \in [0, 1]$ satisfies $f \in [0, 1]$ and $f = 1$ for $\alpha = 1$.

As soon as we use a non-trivial geometry we choose a diffuse interface of *finite width* I_D for the transition between the solid medium $\alpha = 1$ and the surrounding gas / vacuum ($\alpha = 0$). For a relatively large width I_D of the diffuse interface, there are some questions that arise naturally concerning the distribution of the characteristic function α inside the diffuse interface and the resulting effective position of the free surface boundary. In general, it is important to set up the diffuse interface shape such that $\nabla\alpha$ is oriented as the normal vector to the physical surface, i.e. $\nabla\alpha \approx \mathbf{n}$. A simple way to do this is to represent the transition region by a piecewise polynomial. Let $r = r(\mathbf{x})$ be the signed distance between the real physical interface location and a generic point $\mathbf{x}$ under consideration. We then define the shape of the diffuse interface as function of a finite interface thickness $I_D \geq 0$, a shifting parameter η and the auxiliary function:

$$\xi(r) = \begin{cases} 1 & \text{if} \quad r > \quad (1+\eta) I_D, \\ 0 & \text{if} \quad r < -(1-\eta) I_D, \\ \frac{r+(1-\eta) I_D}{2 I_D} & \text{if} \quad r \in [-(1-\eta) I_D, (1+\eta) I_D]. \end{cases} \tag{27}$$

We finally define the solid volume fraction as

$$\alpha(r) = (1 - \xi(r))^p, \tag{28}$$

where $p > 0$ is an exponent that determines the shape of the diffuse interface. The width of the interface I_D should be related to the local size h of the computational mesh, i.e. one would typically choose $I_D \sim h$. In order to reduce I_D as much as possible, we will make use of adaptive mesh refinement (AMR) in combination with a subcell finite volume limiter, as discussed in the next section.

3. Numerical scheme

The numerical method that we use in order to solve the PDE system introduced in the previous Section 2 is an explicit ADER-DG scheme of arbitrary high order of accuracy in space and time on adaptive Cartesian grids (AMR). The numerical method was presented for different PDE systems in [88,87,78], hence in the following we only give a brief summary. The PDE system (9)-(11) can be written in compact matrix-vector notation as

$$\frac{\partial \mathbf{Q}}{\partial t} + \mathbf{B}(\mathbf{Q}) \cdot \nabla \mathbf{Q} = \mathbf{S}(\mathbf{x}, t), \tag{29}$$

where $\mathbf{Q}$ is the state vector, $\mathbf{B}(\mathbf{Q}) \cdot \nabla \mathbf{Q}$ is a non conservative product (see [105,102,103]) and $\mathbf{S}(\mathbf{x}, t)$ is a known source term. In regions where $\alpha = 1$ and thus $\nabla\alpha = 0$, the PDE system (29) reduces to the classical linear elastic wave equations (1), while for $\nabla\alpha \neq 0$ the system becomes locally *nonlinear* and therefore requires a very robust numerical scheme as well as high resolution to be properly solved. Within this paper we use the simple and very robust subcell finite-volume limiter approach in combination with adaptive mesh refinement (AMR). A detailed description of the limiter can be found in [88,87]. As suggested in [88], we employ $N_s = (2N+1)^d$ subgrid cells for the finite volume limiter, where d is the number of space dimensions of the problem and N is the polynomial approximation degree used in the high order ADER-DG scheme. Note that the use of such a fine subgrid within the subcell finite volume limiter does *not* reduce the time step of the overall scheme, since finite volume schemes are stable up to CFL = 1, while DG schemes require CFL $< 1/(2N+1)$. The d-dimensional computational domain Ω is discretized with an adaptive Cartesian grid composed of Cartesian control volumes T_i in space as

$$\Omega = \bigcup_{i=1}^{N_e} T_i, \tag{30}$$

where N_e is the total number of elements. Since we are interested in a high order scheme, we first define a piecewise polynomial nodal basis $\{\phi_k\}_{k=1\ldots(N+1)^d}$ as the set of Lagrange polynomials passing through the Gauss-Legendre quadrature points on a reference unit element T_{ref} for a given polynomial degree $N \geq 0$ and dimension d. A weak formulation of the PDE system is obtained after multiplying Eq. (29) by a test function ϕ_k for $k = 1 \ldots (N+1)^d$ and then integrating over a space-time control volume $T_i \times [t^n, t^{n+1}]$:

$$\int_{t^n}^{t^{n+1}} \int_{T_i} \phi_k \left(\frac{\partial \mathbf{Q}}{\partial t} + \mathbf{B}(\mathbf{Q}) \cdot \nabla \mathbf{Q} \right) d\mathbf{x}\, dt = \int_{t^n}^{t^{n+1}} \int_{T_i} \phi_k \mathbf{S}(\mathbf{x}, t) d\mathbf{x}\, dt. \tag{31}$$

We restrict the discrete solution to the space of piecewise polynomials of degree N, i.e. the numerical solution $\mathbf{u}_h$ is written inside each element T_i in terms of the polynomial basis as

$$\mathbf{u}_h(\mathbf{x}, t^n)\big|_{T_i} = \sum_{k=1}^{(N+1)^d} \phi_k(x) \hat{\mathbf{u}}_{k,i}^n := \phi_k(x) \hat{\mathbf{u}}_{k,i}^n, \tag{32}$$

for $\mathbf{x} \in T_i$ and $i = 1 \dots N_e$. The vector of degrees of freedom of $\mathbf{u}_h(\mathbf{x}, t^n)$ is denoted by $\hat{\mathbf{u}}_i^n$. Throughout the paper we use the Einstein summation convention over repeated indices. Using the definition (32) in the weak formulation given by Eq. (31) we obtain (see also [106,107])

$$\left(\int_{T_i} \phi_k \phi_l d\mathbf{x} \right) \left(\hat{\mathbf{u}}_{l,i}^{n+1} - \hat{\mathbf{u}}_{l,i}^{n} \right) + \int_{t^n}^{t^{n+1}} \int_{\partial T_i} \phi_k \mathcal{D}^-(\mathbf{q}_h^-, \mathbf{q}_h^+) \cdot \mathbf{n} \, dS \, dt + \int_{t^n}^{t^{n+1}} \int_{T_i^\circ} \phi_k \mathbf{B}(\mathbf{q}_h) \cdot \nabla \mathbf{q}_h \, d\mathbf{x} \, dt = \int_{t^n}^{t^{n+1}} \int_{T_i} \phi_k \mathbf{S}(\mathbf{x}, t) \, d\mathbf{x} \, dt, \tag{33}$$

where we have introduced the jump contribution $\mathcal{D}^-(\mathbf{q}_h^-, \mathbf{q}_h^+) \cdot \mathbf{n}$ on the element boundaries and the space-time predictor solution $\mathbf{q}_h(\mathbf{x}, t)$. More details concerning the computation of $\mathbf{q}_h(\mathbf{x}, t)$ will be reported later. For the approximation of the jump term $\mathcal{D}^-$ we use a path-conservative scheme as introduced by Parés in [103] and Castro et al. in [102]. We introduce a Lipschitz continuous path function $\psi(\mathbf{q}_h^-, \mathbf{q}_h^+, s)$ defined for $s \in [0, 1]$ such that $\psi(\mathbf{q}_h^-, \mathbf{q}_h^+, 0) = \mathbf{q}_h^-$ and $\psi(\mathbf{q}_h^-, \mathbf{q}_h^+, 1) = \mathbf{q}_h^+$, where $\mathbf{q}_h^-$ denotes the boundary-extrapolated state from within the element T_i and $\mathbf{q}_h^+$ the boundary-extrapolated state from the neighbor element. The simplest possible choice for ψ, which we use in this paper, is the linear segment path between the two states $\mathbf{q}_h^-$ and $\mathbf{q}_h^+$:

$$\psi(\mathbf{q}_h^-, \mathbf{q}_h^+, s) = \mathbf{q}_h^- + s \left(\mathbf{q}_h^+ - \mathbf{q}_h^- \right). \tag{34}$$

Following [105,103,102] we now define the jump contribution $\mathcal{D}^-(\mathbf{q}_h^-, \mathbf{q}_h^+) \cdot \mathbf{n}$ so that it satisfies the generalized Rankine-Hugoniot conditions

$$\mathcal{D}^-(\mathbf{q}_h^-, \mathbf{q}_h^+) \cdot \mathbf{n} + \mathcal{D}^+(\mathbf{q}_h^-, \mathbf{q}_h^+) \cdot \mathbf{n} = \int_0^1 \mathbf{B}(\psi(\mathbf{q}_h^-, \mathbf{q}_h^+, s)) \cdot \mathbf{n} \frac{\partial \psi}{\partial s} ds. \tag{35}$$

The previous path integral can simply be evaluated *numerically* using a sufficient number of Gaussian quadrature points. As Riemann solver we use the new HLLEM-type Riemann solver for non-conservative systems recently described in [92], since we want to exactly preserve the contact discontinuities of the material parameters and of the volume fraction function that appear in the PDE system. At this point we would like to emphasize that in this paper we deliberately use finite volume and discontinuous Galerkin finite element schemes that employ a piecewise polynomial approximation space, which explicitly permits *jumps* in the discrete solution at element interfaces. In this context the path-conservative schemes can properly deal with jumps in α if they are *exactly* resolved at an element interface, thus naturally allowing to discretize problems also with $I_D = 0$, see also [102,103] for a discussion in the context of shallow water equations with discontinuous bottom topography. In the case of $I_D = 0$, our method becomes again a sharp interface method if the jumps are exactly resolved on the grid, but this is actually *not* the main objective of the present paper.

Regarding the space-time predictor, we need to introduce a new polynomial basis of degree N in space and time $\{\theta_k\}_{k=1\dots(N+1)^{d+1}}$ where now $\theta_k(\mathbf{x}, t)$ contains also the time. We represent $\mathbf{q}_h(\mathbf{x}, t)$ in terms of this new space-time basis as

$$\mathbf{q}_h(\mathbf{x}, t) = \sum_{k=1}^{(N+1)^{d+1}} \theta_k(\mathbf{x}, t) \hat{\mathbf{q}}_k^n. \tag{36}$$

Let $T_i^\circ = T_i - \partial T_i$ denote the interior of T_i and $T_i^{st} = T_i^\circ \times [t^n, t^{n+1}]$ denote the new space-time control volume. The space-time predictor is then computed as an element-local solution of the following weak formulation of the PDE system (29):

$$\int_{T_i^{st}} \theta_k \frac{\partial \mathbf{q}_h}{\partial t} d\mathbf{x} \, dt + \int_{T_i^{st}} \theta_k \mathbf{B}(\mathbf{q}_h) \cdot \nabla \mathbf{q}_h d\mathbf{x} \, dt = \int_{T_i^{st}} \theta_k \mathbf{S}(\mathbf{x}, t) d\mathbf{x} \, dt, \tag{37}$$

for $k = 1 \dots (N+1)^{d+1}$. Using integration by parts in the first term of Eq. (37) we obtain two spatial contributions on T_i at t^{n+1} and t^n and an internal one since $\theta_k = \theta_k(\mathbf{x}, t)$ contains explicitly the time. For the spatial contribution at time t^n we use the numerical solution from the previous time step. Notice that this corresponds to upwinding in the time direction due to the causality principle. One thus obtains the following weak formulation of the PDE *in the small* [108]:

$$\int_{T_i} \theta_k(\mathbf{x}, t^{n+1}) \mathbf{q}_h(\mathbf{x}, t^{n+1}) d\mathbf{x} - \int_{T_i} \theta_k(\mathbf{x}, t^n) \mathbf{u}_h(\mathbf{x}, t^n) d\mathbf{x} - \int_{T_i^{st}} \frac{\partial \theta_k}{\partial t} \mathbf{q}_h(\mathbf{x}, t) d\mathbf{x} \, dt + \int_{T_i^{st}} \theta_k \mathbf{B}(\mathbf{q}_h) \cdot \nabla \mathbf{q}_h d\mathbf{x} \, dt = \int_{T_i^{st}} \theta_k \mathbf{S}(\mathbf{x}, t) d\mathbf{x} \, dt. \tag{38}$$

Since Eq. (38) is element-local it can be solved using a simple and efficient Picard method without any communication with the neighbor elements, see e.g. Dumbser et al. [109].

The numerical scheme is constrained by a *local* CFL-type stability condition, see [109,110,87], that is given by

$$\Delta t < \frac{\mathrm{CFL}}{d} \frac{h}{2N+1} \frac{1}{|\lambda_{max}|}, \tag{39}$$

where h is the local mesh size, λ_{max} is the maximum eigenvalue of the PDE system, and CFL< 1 is the Courant number, which should be chosen according to [109] in order to have linear stability. Concerning the adaptive mesh refinement (AMR) we rely on the ExaHyPE engine http://exahype.eu, which is built upon the space-tree implementation Peano [111, 112] realizing cell-by-cell refinement [113]. For further details about AMR in combination with high order finite volume and DG schemes with time-accurate local time stepping (LTS) used in this work, see [110,114–116]. Throughout this paper, we use adaptive meshes with a refinement factor of $\mathfrak{r} = 3$ between two adjacent levels of refinement. In order to illustrate the useful combination of AMR with the subcell finite volume limiter, we provide the following example: with two levels of mesh refinement and for a DG scheme with polynomial approximation degree $N = 3$, the finite volume subgrid on the finest AMR level will be by a factor of $\mathfrak{r}^2 \cdot (2N+1) = 3^2 \cdot (2 \cdot 3 + 1) = 63$ finer than the grid used for the DG scheme on the coarsest grid level. This corresponds to a mesh refinement of almost two orders of magnitude. However, this has no negative impact at all on the time step size used on the coarsest grid level, thanks to the use of time-accurate local time stepping (LTS), which is straightforward for ADER discontinuous Galerkin and ADER finite volume schemes, see [36,110,87]. The combination of AMR with the fine subgrid used for the finite volume limiter is necessary to alleviate the loss of formal order of accuracy inside the limited cells and in order to allow a small interface width $I_D \sim h$.

In order to decide where to refine, we introduce a simple refinement indicator function named $\varphi = \varphi(\mathbf{x}, t)$ that defines the observed variable for the refinement/recoarsening process and a so called real-valued *estimator function* $\chi = \chi[\varphi]$, see again [110] for more details. After defining the indicator function, we define the cell-averages of φ as

$$\hat{\varphi}_i = \frac{1}{|T_i|} \int_{T_i} \varphi(\mathbf{x}, t)\, d\mathbf{x} \qquad \forall i = 1 \dots N_e, \tag{40}$$

and then we compute the estimator function as

$$\chi_i[\varphi] = \max_{c \in \mathcal{V}_i} \left(\left| \hat{\varphi}_c - \hat{\varphi}_i \right| / \left\| \mathbf{x}_c - \mathbf{x}_i \right\| \right), \tag{41}$$

where $\mathcal{V}_i$ contains all the Voronoi neighbor elements of T_i. Our estimator function χ is simply based on an approximation of the gradient of the solution in several spatial directions [110]. With these ingredients at hand, we introduce a simple rule for the refinement/recoarsening process based on two thresholds χ^+ and χ^- as follows:

(i) if $\chi_i[\varphi] > \chi^+$ then T_i is labeled for mesh refinement;
(ii) if $\chi_{[}\varphi] < \chi^-$ then T_i is labeled for mesh recoarsening.

Within this paper, we always use $\varphi(\mathbf{x}, t) = \varphi(Q) = \alpha$, $\chi^+ = 0.01$ and $\chi^- = 0.001$. We will also use the volume fraction α to specify the zones where to activate the subcell finite volume limiter [88]. In particular, we activate the FV limiter whenever $\alpha \notin [\epsilon, 1-\epsilon]$, with $\epsilon = 10^{-3}$. As long as the topology of the geometry described by α is supposed to be stationary in time, we can consider the refinement and the limited zones also as steady and therefore they need to be identified only once in the mesh initialization step.

We stress again that the use of a time-accurate local time stepping strategy (LTS) is mandatory in order to avoid the reduction of the time step size Δt in regions that are far away from the diffuse interface.

4. Numerical results

4.1. Reflected plane wave

The purpose of this first test problem is to systematically study the influence of the width I_D of the diffuse interface layer onto the numerical results. We also show that the model indeed converges to the correct solution in the limit $I_D \to 0$. We take a simple plane wave impulse in a domain $\Omega = [-1, 1] \times [-0.1, 0.1]$ initially placed at $x_0 = -0.25$ and hitting a free surface boundary placed in $x_D = 0$. The Lamé constants are chosen as $\lambda = 2$, $\mu = 1$ and $\rho = 1$. We define $\mathbf{Q}_0 = (0, 0, 0, 0, 0, 0, 0, 0, 0, 0, \lambda, \mu, \rho, \alpha(x))$ and $\boldsymbol{\delta} = (0.4, 0.2, 0.2, 0, 0, 0, -0.2, 0, 0, 0, 0, 0, 0, 0)$ and set

$$\mathbf{Q}(x, y, t = 0) = \mathbf{Q}_0 + \boldsymbol{\delta} \cdot e^{-\frac{(x-x_0)^2}{\epsilon^2}},$$

with the halfwidth $\epsilon = 0.05$. The volume fraction function $\alpha(x)$ is prescribed according to (28) and (27). We use an ADER-DG P_4 scheme and a uniform Cartesian grid with 100×2 elements. The mesh resolution is chosen fine enough so that the

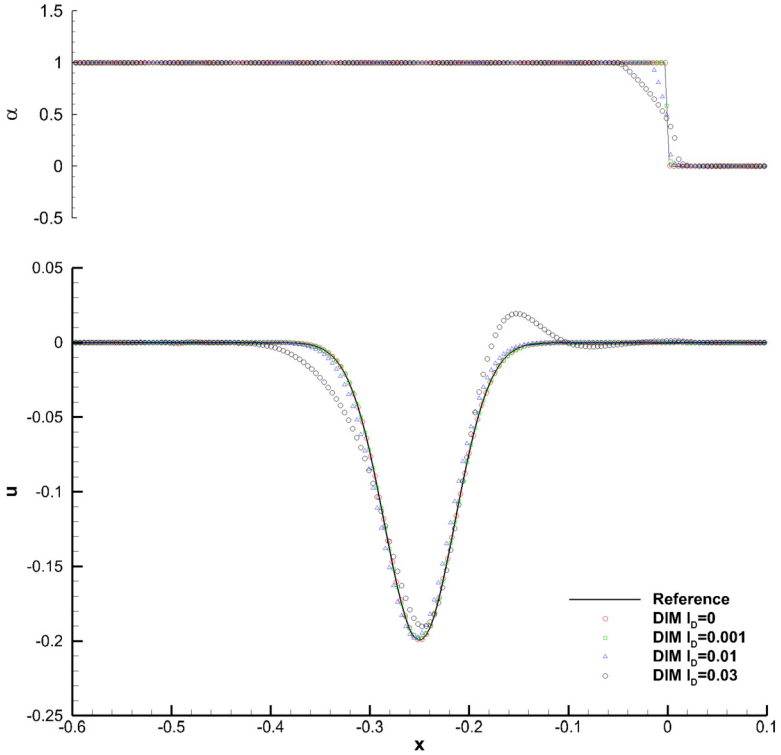

Fig. 1. Numerical results obtained with the new diffuse interface approach for a plane wave reflection problem on a free surface located in $x = 0$ using a variable interface thickness of $I_D = 0$, $I_D = 0.001$, $I_D = 0.01$ and $I_D = 0.03$. In all four cases we report the velocity component u compared with the exact solution of the problem (bottom) together with the spatial distribution of α (top).

numerical results are grid-independent and only depend on the choice of the interface thickness I_D. Since for this test $c_p = 2$, the exact solution at time $t = t_{end} = 0.25$ is the reflected p-wave which is located again in the initial position. We consider four cases with different choices of the interface width I_D, ranging from $I_D = 0.03$ to the limit $I_D = 0$, where the interface is exactly located on a cell boundary. From the results depicted in Fig. 1 we can conclude that the diffuse interface method is able to reproduce the exact solution of the problem for sufficiently small values of the interface thickness I_D. We also stress that the use of a path-conservative method allows us to reduce the interface thickness exactly to $I_D = 0$, which leads to a jump in α at an element interface, but which is still properly accounted for thanks to the jump terms $\mathcal{D}^-$ used in the numerical scheme.

For rather large values of the finite interface thickness I_D, where the actual shape of the spatial distribution of α starts to play a role, we have found empirically that a good choice for the parameters η and p in (27) is $\eta = -0.6$ and $p = 0.5$. This choice allows to obtain still a correct reflection of a p-wave even for very thick interfaces. However, for sufficiently small values of I_D, the choice of η and p has only very little influence. We consider now a similar setup of a p-wave traveling in a heterogeneous material with periodic boundaries everywhere. The Lamé constants are specified as

$$(\lambda, \mu, \rho) = \begin{cases} (4, 0, 1) & 0 \le x \le 0.2 \\ (2, 1, 1) & \text{otherwise} \end{cases} \tag{42}$$

Note that in the area $0 \le x \le 0.2$ the Poisson ratio is $\nu = 1/2$. The ability of ADER-DG schemes to deal with fluids ($\mu = 0$) properly has already been discussed in [34,117]. We furthermore place a reflective free surface at $x_{fs} = 0.75$ only by using a change in the parameter α so that the exact solution at $t_{end} = 1.0$ is again the reflected p-wave, located in the initial position. We use an ADER-DG P_3 scheme on a sequence of uniform Cartesian grids in order to check the accuracy of the scheme. In Table 1 we report the L_2-error norm in the case where no free surface boundary appears (i.e. $\alpha = 1$ everywhere). In this case the wave passes through the heterogeneous material and returns to the initial state due to the periodic boundary. We observe high order of convergence if we use a pure DG scheme without limiter (left column), while we observe the expected decay of the order if we artificially activate the limiter close to $x = x_{fs}$. Taking $\alpha = 0$ for $x \ge x_{fs}$, we observe a first order of convergence, since the jump in α also represents a jump in the discrete solution, see Table 2. This is observed also for positive values of I_D and different values of ϵ_0, as reported in the right column of Table 2.

In principle one can keep the Lamé parameters inside the diffuse interface and outside the solid as the ones inside the solid. However we have empirically found out that rescaling the Lamé constants according to the local value of α improves the numerical convergence and allows to reach second order of accuracy, see Table 3.

Table 1
Computed L_2-error norm for the case $\alpha = 1$ without the limiter (left) and limiting the elements that are close to x_{fs} (right).

Elements	$\epsilon_{L_2}(u)$	
20×2	4.8988e-3	–
40×2	7.2321e-4	2.8
80×2	4.1602e-5	4.1
160×2	2.4629e-6	4.1

Elements	$\epsilon_{L_2}(u)$	
20×2	6.6547e-3	–
40×2	1.3748e-3	2.3
80×2	2.1391e-4	2.7
160×2	3.7588e-5	2.5

Table 2
Computed L_2-error norm for the case of α aligned with the mesh (left) and for positive diffuse interface size I_D (right).

Elements	$\epsilon_{L_2}(u)$	
320×2	2.5851e-4	–
640×2	1.2104e-4	1.1
1280×2	4.6230e-5	1.4
2560×2	2.0770e-5	1.2

Elements	I_D	$\epsilon_{L_2}(u)$, $\epsilon_0 = 10^{-3}$		$\epsilon_{L_2}(u)$, $\epsilon_0 = 10^{-4}$	
40×2	0.02	3.4813e-3	–	3.2060e-3	–
80×2	0.01	2.0510e-3	0.8	2.0144e-3	0.7
160×2	0.005	1.1723e-3	0.8	1.1374e-3	0.8
320×2	0.0025	5.9087e-4	1.0	5.9268e-4	0.9

Table 3
Computed L_2-error norm for α aligned with the mesh and rescaled Lamé constants λ and μ.

Elements	$\epsilon_{L_2}(u)$	
40×2	1.4512e-2	–
80×2	2.0014e-4	2.9
160×2	3.2374e-5	2.6
320×2	8.9161e-6	1.9

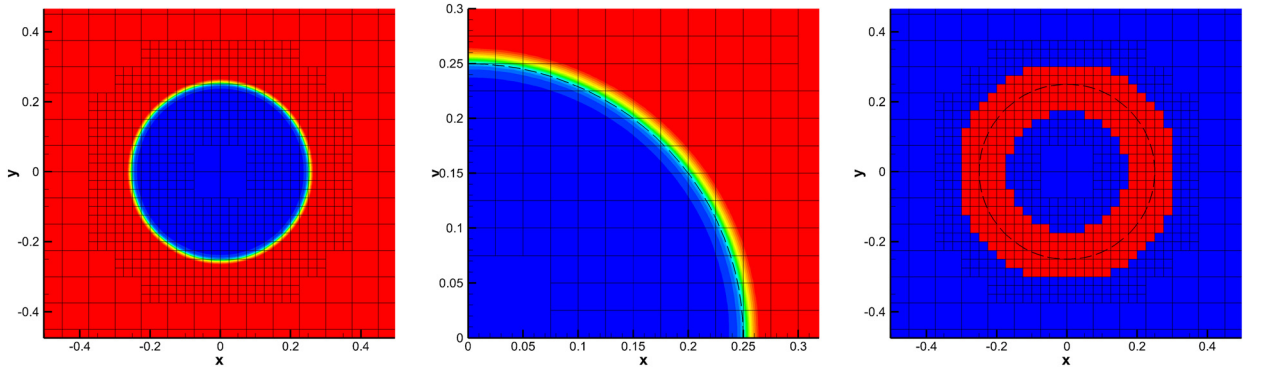

Fig. 2. Setup of the scattering test problem. AMR grid and distribution of the characteristic function α (left). Detail of the free surface location ∂C shown via a dashed line and α color contours (center). Limited cells highlighted in red and unlimited cells shown in blue (right). (For interpretation of the colors in the figure(s), the reader is referred to the web version of this article.)

4.2. Scattering of a plane wave on a circular cavity

In this test case we consider an initially planar p-wave traveling in x-direction inside a solid medium and hitting an empty circular cavity. The initial state is given by

$$\mathbf{Q}(x,0) = (0,0,0,0,0,0,0,0,0,\lambda,\mu,\rho,\alpha) + 0.1 \cdot (4,2,2,0,0,0,-2,0,0,0,0,0,0,0)\sin(2\pi x), \tag{43}$$

with $\lambda = 2$, $\mu = 1$ and $\rho = 1$. The value of α is parameterized through the circular surface $C = \{(x,y) \mid x^2 + y^2 \leq 0.25^2\}$ so that $\alpha(\mathbf{x}) = 0$ if $\mathbf{x} \in C$ and $\alpha = 1$ if $\mathbf{x} \notin C$. The width parameter of the diffuse interface is set to $I_D = 0.01$ on ∂C. The computational domain is $\Omega = [-3,3]^2$ and the initial Cartesian grid at level $\ell = 0$ consists of 80×80 cells. We then use one further refinement level $\ell_{max} = 1$ based on the gradient of α in order to refine the mesh close to the diffuse interface. Furthermore, we use a fifth order ADER-DG method based on piecewise polynomials of degree $N = 4$ in both space and time, supplemented with a second order TVD subcell finite volume limiter. The resulting AMR grid and the color contours of α are shown in Fig. 2, together with the region where the subcell finite volume limiter is activated. From the plot in the central panel of Fig. 2 one can see that the width of the interface layer is of the order of the size of one cell of the high order DG scheme.

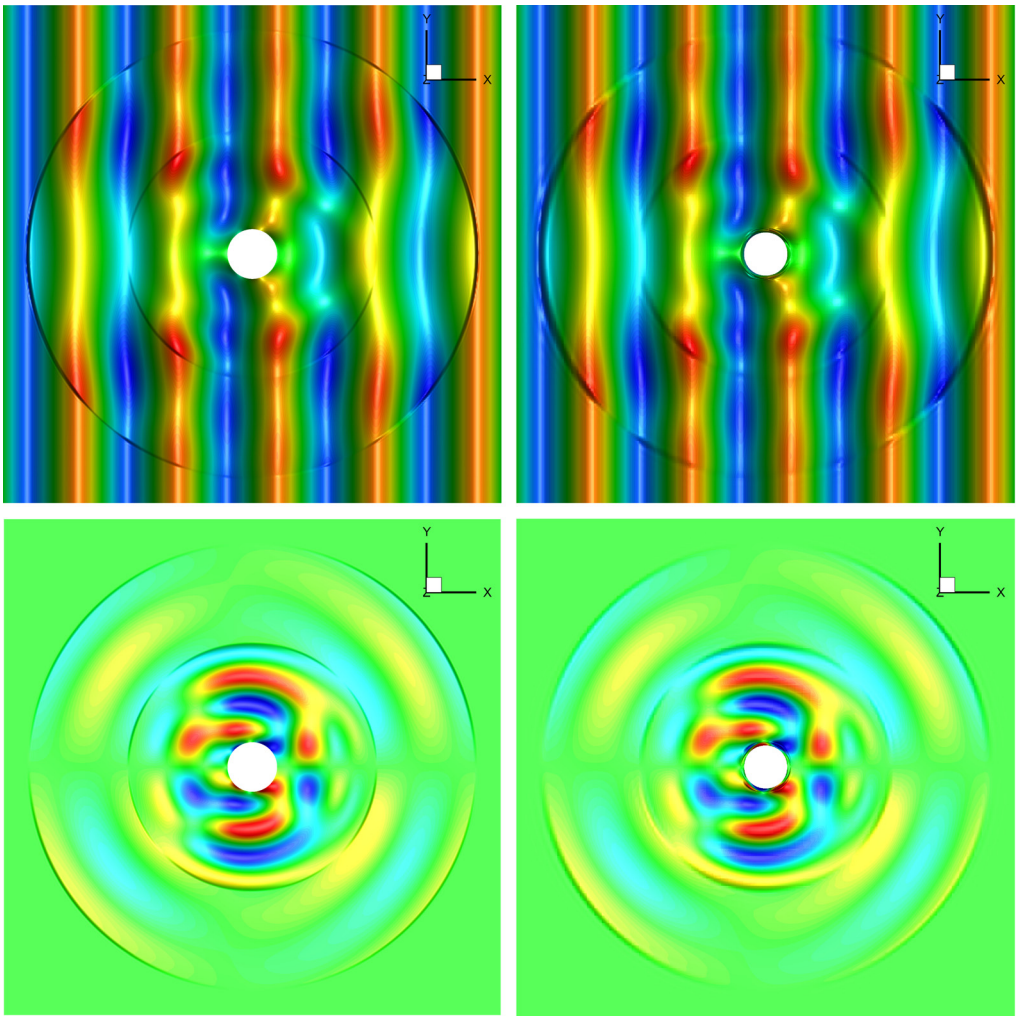

Fig. 3. 2D wave scattering problem at time $t = 1$. Reference solution (left) and solution obtained with the new diffuse interface approach on AMR grid (right) for σ_{xx} (top) and σ_{xy} (bottom).

In Fig. 3 we report the numerical results obtained with the new diffuse interface approach on adaptive Cartesian grids at time $t = 1$ and compare them with a reference solution that has been obtained with a third order ADER-DG scheme ($N = 2$) on a very fine unstructured boundary-fitted mesh [118] composed of $N_e = 563,280$ triangles. Fig. 4 shows a comparison between the reference solution and the numerical solution obtained with the diffuse interface method via numerical seismograms that have been recorded in two receiver locations $\mathbf{x}_1 = (0.5, 0.5)$ and $\mathbf{x}_2 = (1.0, 0.0)$. A very good agreement between the new diffuse interface method and the reference solution is obtained for this test case.

At this point we would like to stress again that in the new diffuse interface approach, the presence of the boundary condition is included in the PDE system *only* by choosing a spatially variable value of α. The AMR grid is *not* at all aligned with the free surface boundary and remains always locally Cartesian (with h-adaptivity). Furthermore, the time step size in our approach is *not* affected by the so-called small cell problem or sliver element problem, as it would have been the case for Cartesian cut-cell methods or low quality unstructured meshes and which usually requires a special treatment [36,49]. In our diffuse interface approach, the eigenvalues of the PDE system are independent of α and also our mesh can be chosen independently of α and almost independently of the geometry of the problem to be solved (apart from local h adaptivity used in regions of strong gradients of α). Therefore, the admissible local time step size is only governed by the maximum wave speed c_p and the local mesh size of the AMR grid, and not by the geometry of the problem to be solved. Note that in all our simulations on AMR grids, we use time-accurate local time stepping (LTS), see [36,110,119,87] for details.

4.3. 2D tilted Lamb problem

In this test case we to study the two dimensional tilted Lamb problem. We take the same setup as used in [25,118,49]. The physical domain $\Omega = \{(x, y) \in \mathbb{R}^2 \,|\, 0 \leq x \leq 4000\ ,\ 0 \leq y \leq 2000 + \tan(\theta)x\}$ contains a free surface with a tilt angle of

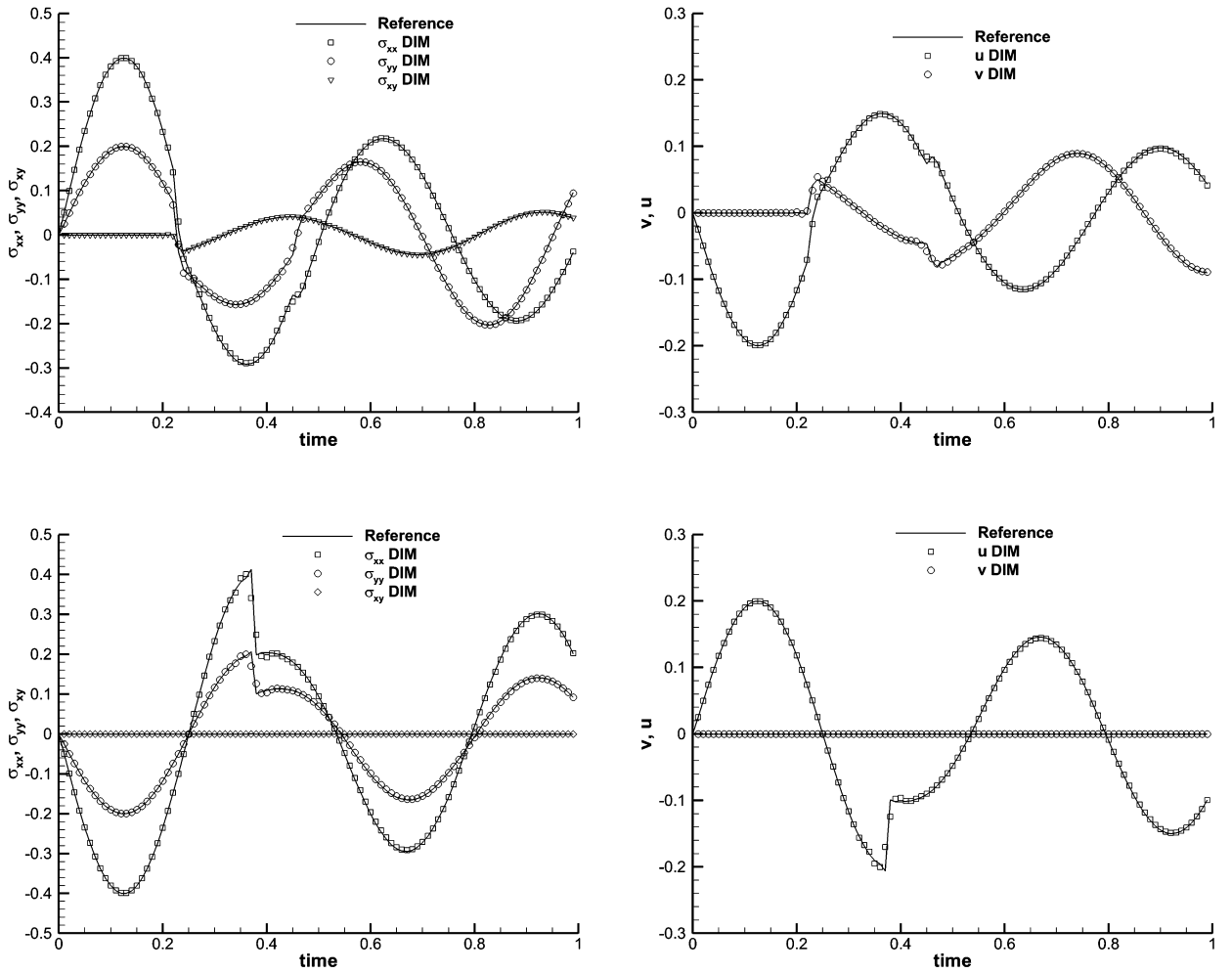

Fig. 4. 2D wave scattering problem. Comparison between the reference solution and the numerical results obtained with the new diffuse interface method on AMR grid for two seismograms recorded in $\mathbf{x}_1 = (0.5, 0.5)$ (top row) and $\mathbf{x}_2 = (1.0, 0.0)$ (bottom row).

$\theta = 10°$, so that the boundary is *not grid aligned* along the coordinate axes when using a Cartesian mesh. The computational domain used for the diffuse interface approach, however, is a simple rectangular box that fully contains Ω. The initial Cartesian grid on the coarsest level $\ell = 0$ has 96×90 cells and we use an ADER-DG P_3 scheme with subcell finite volume limiter to solve this problem. The chosen $p-$ and $s-$wave velocities are set to $c_p = 3200\ \mathrm{m\,s^{-1}}$ and $c_s = 1847.5\ \mathrm{m\,s^{-1}}$, respectively. The mass density is taken as $\rho = 2200\ \mathrm{kg\,m^{-3}}$ so that the resulting Lamé constants are $\lambda = 7.5096725 \cdot 10^9$ and $\mu = 7.50916375 \cdot 10^9$. The initial condition is $\mathbf{Q}(\mathbf{x}, 0) = 0$ everywhere in Ω. The wave propagation is driven by a directional point source located in $\mathbf{x}_s = (1720.0, 2265.28)$. We place two receivers, one close to the interface but slightly below, so that $\alpha = 1$, $\mathbf{x}_2 = (2694.96, 2460.08)$ and the other one exactly at the physical interface in $\mathbf{x}_1 = (2694.96, 2475.08)$. As reference solution we use again an ADER-DG method on boundary-fitted unstructured meshes, which has already been carefully validated against the exact solution of Lamb's problem in [118]. The reference solution is computed using a polynomial approximation degree $N = 4$ in space and time and an unstructured mesh of $N_e = 844,560$ triangles. The point source

$$S(\mathbf{x}, t) = \frac{1}{\rho} \vec{\boldsymbol{d}} \delta(\mathbf{x} - \mathbf{x}_s) \mathcal{S}(t)$$

is a delta distribution in space located in $\mathbf{x} = \mathbf{x}_s$ and its temporal part is a Ricker wavelet given by

$$\mathcal{S}(t) = a_1 \left(0.5 + a_2 (t - t_D)^2 \right), \tag{44}$$

where $t_D = 0.08$ s is the source delay time; $a_1 = -2000\ \mathrm{kg\,m^{-2}\,s^{-2}}$; $a_2 = -(\pi f_c)^2$; and $f_c = 14.5$ Hz. Finally the vector $\vec{\boldsymbol{d}} = (-\sin\theta, \cos\theta, 0, 0, 0, 0, 0, 0, 0, 0)^\top$ determines the direction of the impulse and takes into account the tilt angle θ. For this test we use an interface thickness of $I_D = 2$ m. Furthermore we compare two different resolutions at the interface

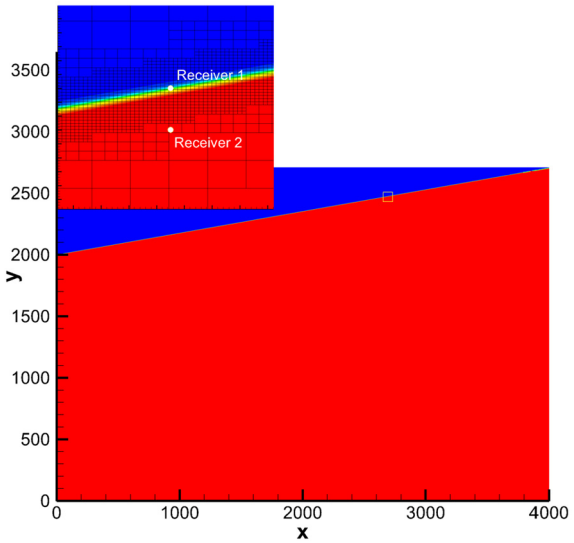

Fig. 5. Tilted Lamb problem. Distribution of α in the computational domain and position of the two receivers. Note that the tilted free surface is not aligned with the Cartesian grid. The resolution of the free surface is improved by a combination of AMR and subgrid finite volume limiter.

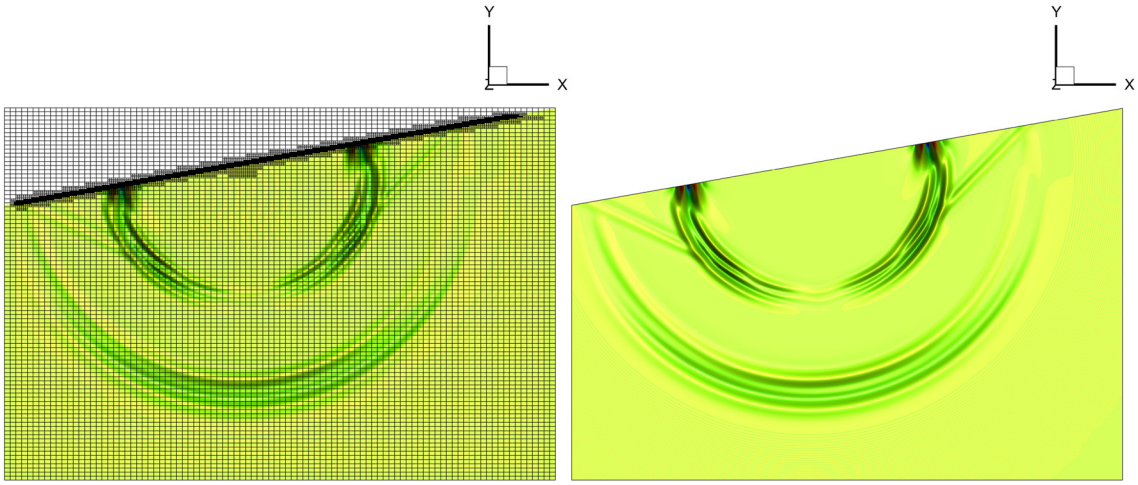

Fig. 6. Tilted Lamb problem. Comparison of the vertical velocity v between the new diffuse interface approach on AMR grid (left) and the reference solution obtained on a boundary-fitted unstructured mesh (right) at $t = 0.6$.

corresponding to a maximum refinement level of $\ell_{max} = 2$ and $\ell_{max} = 3$. Fig. 5 shows the value of the solid volume fraction α, as well as the positions of the seismogram recorders in $\mathbf{x}_1$ and $\mathbf{x}_2$. In Fig. 6 we compare between the numerical solution obtained with the new diffuse interface approach on Cartesian AMR grids and the reference solution obtained on a boundary-fitted unstructured mesh. We can observe a good agreement between the two solutions, which becomes also clear if we compare the seismograms, see Fig. 7. In this case it is also evident that the use of a higher grid resolution at the interface allows to approach the reference solution better.

In this last part and as an outlook towards future work on nonlinear large-strain elasto-plasticity, we increase the energy of the point source by setting $a_1 = -2 \cdot 10^{11}\ \mathrm{kg\,m^{-2}\,s^{-2}}$ and we now allow the diffuse interface to *move* according to the local velocity field, i.e. instead of solving $\partial\alpha/\partial t = 0$ we simply solve

$$\frac{\partial \alpha}{\partial t} + \boldsymbol{v} \cdot \nabla \alpha = 0. \tag{45}$$

The resulting numerical solution at $t = 0.6$ is shown in Fig. 8. Here the solution is similar in the internal part of the domain, however, if we zoom close to the free surface (see again Fig. 8) we can clearly see how the elastic waves deform the geometry of the free-surface boundary. The time history of this deformation is shown in Fig. 9, where we plot the iso-line $\alpha = 0.5$ that shows the deformation of the solid medium via the color function α.

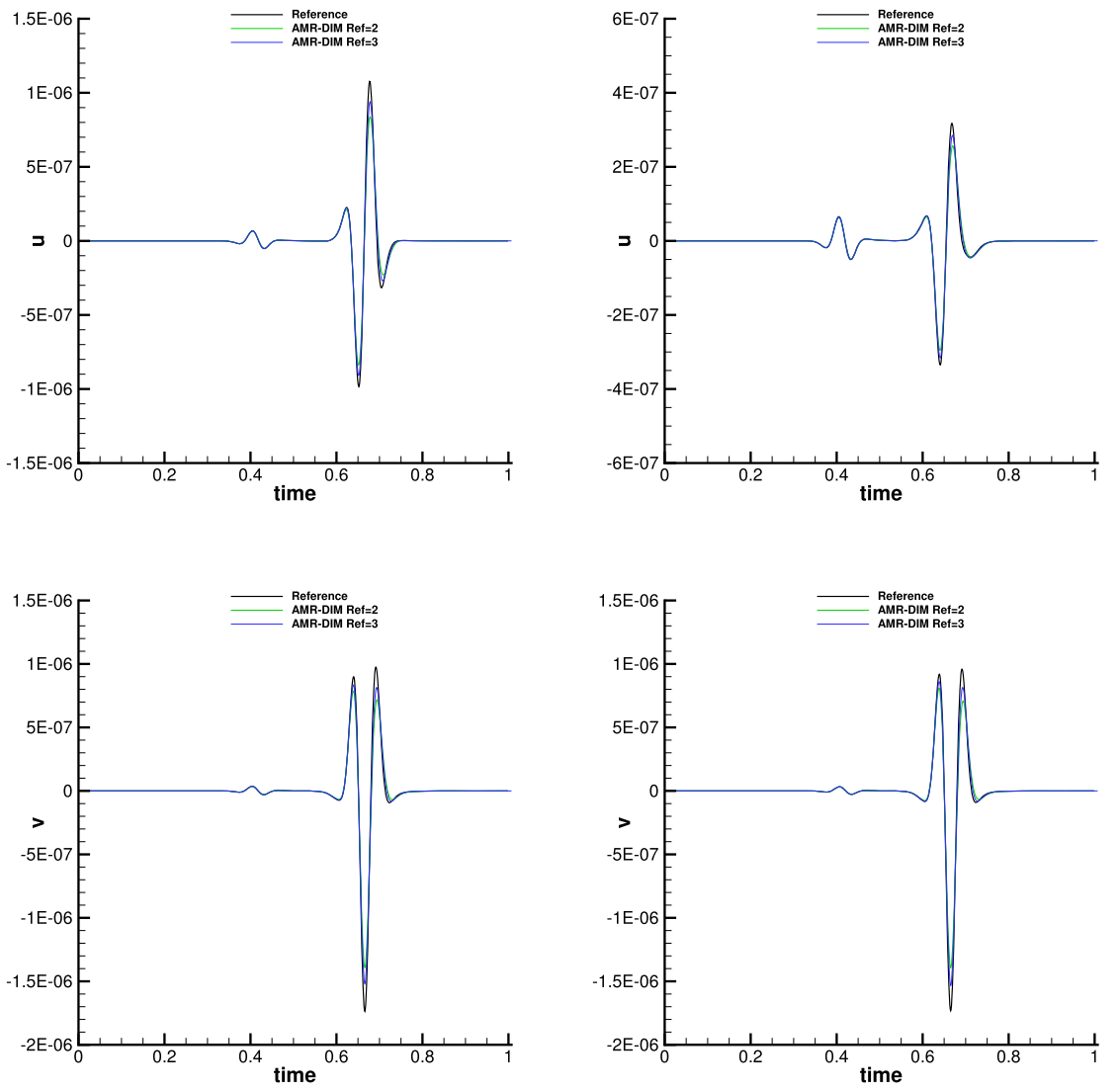

Fig. 7. Lamb's problem. Comparison of the reference solution (solid black line) and the numerical solution obtained with the new diffuse interface approach on adaptive Cartesian grids for 2 and 3 refinement levels in the two receivers 1 (left) and 2 (right).

4.4. Wave propagation in a complex 2D geometry

This test is very similar to the tilted Lamb problem but in a non-trivial domain with heterogeneous material. The domain is $\Omega_f = \{(x, y) \mid x \in [0, 4000]\ y \in [0, f(x)]\}$ where $f(x) = 2000 + 100\left(\sin(\frac{3}{200}x) + \sin(\frac{2}{200}x)\right)$ describes the upper topography. Free surface boundary conditions are imposed everywhere on $\partial\Omega_f$. The heterogeneous material consists in two layers whose parameters are reported in Table 4. The initial state vector is $\mathbf{Q}(x, 0) = 0$ and the wave propagation is driven by a point source placed in $\bar{\mathbf{x}} = (3000, 1500.18)$ as described in the previous Section 4.3. Three seismometers are placed in the locations reported in Table 5 and graphically depicted in Fig. 10 to record the time history of the wave propagation. We take an extended domain $\Omega = [-50, 4050] \times [-50, 2300]$ that fully contains Ω_f. The initial Cartesian grid on level $\ell = 0$ is composed of 160×90 elements. Subsequently, one refinement level is added in regions with large gradients of α, i.e. we set $\ell_{max} = 1$. The value of α is used to define the complex physical domain Ω_f following our diffuse interface approach. The chosen smoothing parameter close to the upper surface is taken as $I_D = 5.0$, based on the distance function from a point and the boundary of the domain $\partial\Omega_f$. We furthermore use $I_d = 0$ on the left, right and bottom boundaries, which are all grid aligned. The resulting AMR grid and the spatial distribution of α in the computational domain are shown in Fig. 10. A direct comparison between the solution obtained with the novel diffuse interface approach using an ADER-DG P_4 scheme on the AMR grid and the reference solution obtained with an ADER-DG P_4 scheme on a boundary-fitted unstructured mesh composed of 20254 triangles is reported in Fig. 11. The comparison of the seismograms at the three receivers

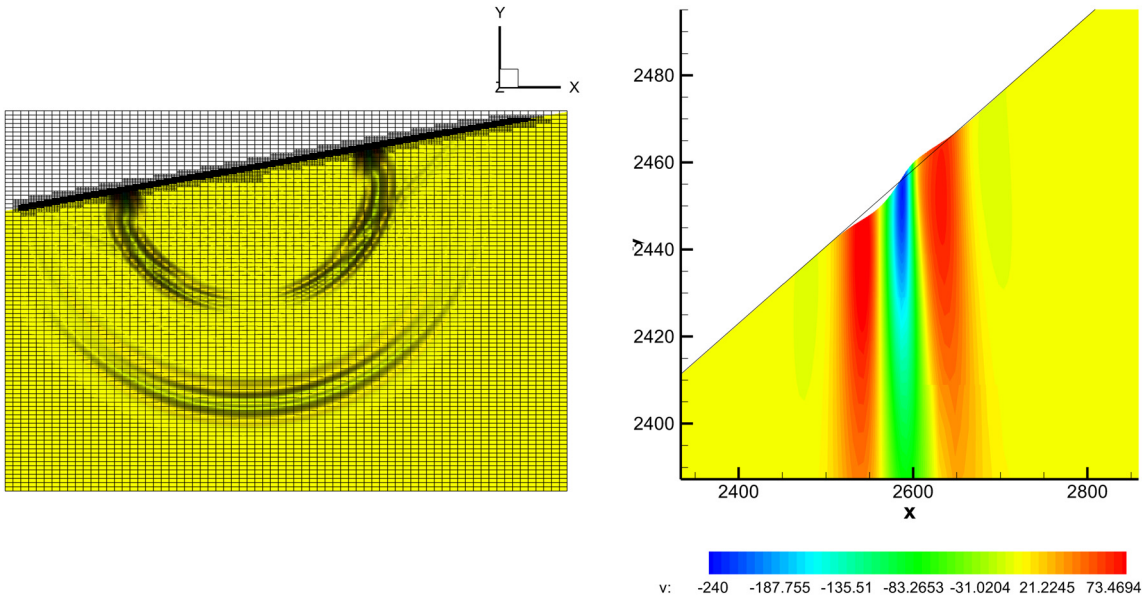

Fig. 8. Lamb's problem with moving free surface boundary. Mesh and numerical solution v (left). Profile of $\alpha = 0.5$ at $t = 0.6$ compared with the initial configuration (right).

up to $t = 2.0$ s is shown in Figs. 12 and 13. A very good agreement is achieved for short times, and even at later times the agreement remains rather good, considering that at later times the signal is the result of several reflected waves on the free surface.

The time series of the resulting total energy up to a longer time $t_{end} = 25$ and the time series of the velocity u in the fourth receiver are shown in Fig. 14. It is clear from Fig. 14 that, after the initial release of the energy, the numerical method in combination with the new mathematical model proposed in this paper *dissipates* energy and does not show any kind of instabilities, even for a long time simulation.

4.5. Scattering of a planar wave on a sphere

Here we consider the 3D extension of the test reported in Section 4.2, which consists of a planar $p-$wave traveling in the $x-$direction and hitting a spherical cavity on which free surface boundary conditions apply. Our computational domain is the simple cube $\Omega = [-3, 3]^3$ and the presence of the spherical obstacle is only taken into account by a spatially variable distribution of the volume fraction function α. So $\alpha = 1$ if $\alpha \notin B$ and $\alpha = 0$ if $\alpha \in B$ where $B = \{(x, y, z) \mid x^2 + y^2 + z^2 \leq 0.25^2\}$ is the sphere with radius $R = 0.25$. The chosen interface width is $I_D = 10^{-2}$. The computational domain is covered with a uniform initial mesh of $40 \times 40 \times 40$ elements. We then add one refinement level $\ell_{max} = 1$ based on the gradient of α. Furthermore we use piecewise polynomials of degree $N = 5$ in space and time for this simulation. We consider three receivers placed in $\mathbf{x}_1 = (-1, 0, 0)$, $\mathbf{x}_2 = (0, -1, 0)$ and $\mathbf{x}_3 = (0.5, 0.5, 0.5)$. As a reference solution we use again the explicit ADER-DG scheme implemented in the `SeisSol` code [35,120,121] using a boundary-fitted unstructured grid with $N_e = 31,732$ tetrahedral elements and piecewise polynomials of degree $N = 4$ in space and time. `SeisSol` is a mature production code for large-scale seismic wave propagation problems in complex 3D geometries and has been heavily optimized so that it achieves a sustained Petaflop performance on modern supercomputers, see [120,121] and `www.seissol.org`. A comparison of the contour colors for the velocity component w is shown in Fig. 15 and a direct comparison of the time series recorded in the three receivers is presented in Fig. 16. A very good agreement between the reference solution and the novel diffuse interface approach can be observed also in this case. We stress that the geometry of the sphere is not aligned with the adaptive Cartesian mesh that was employed to carry out this simulation.

4.6. 3D Layer Over Halfspace (LOH.1)

We now apply the diffuse interface method proposed in this paper to a classical 3D benchmark problem originally presented and discussed by S.M. Day in the final report to the Pacific Earthquake Engineering Research Center concerning tests of 3D elastodynamics codes, see [122]. The setup of the test problem called *Layer Over Halfspace* (LOH.1) is also similar

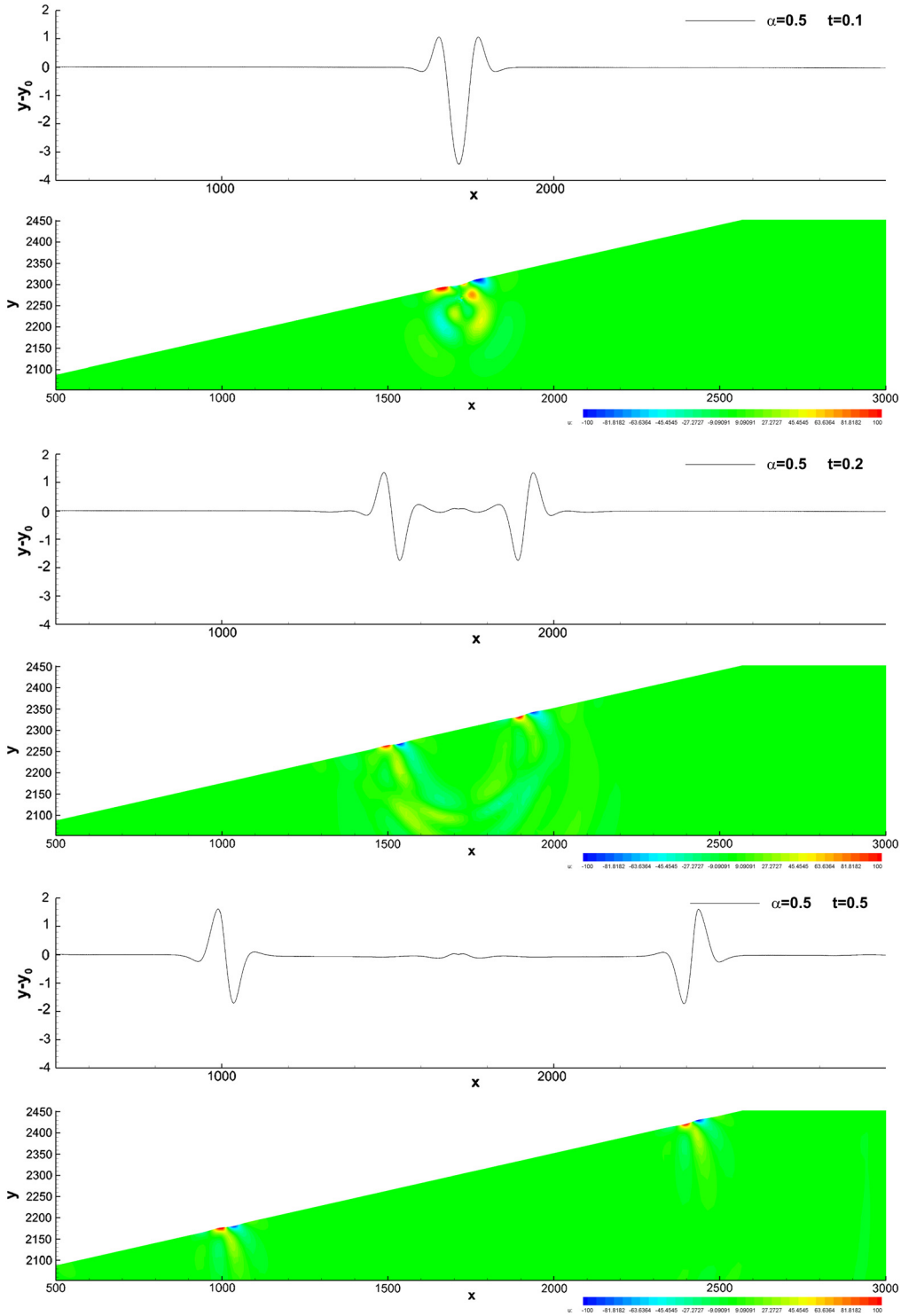

Fig. 9. Lamb's problem with moving free surface boundary. Displacement of the free surface (computed from the curve $\alpha = \frac{1}{2}$) and velocity component u at times $t = 0.1$, $t = 0.2$ and $t = 0.5$, respectively, from top to bottom.

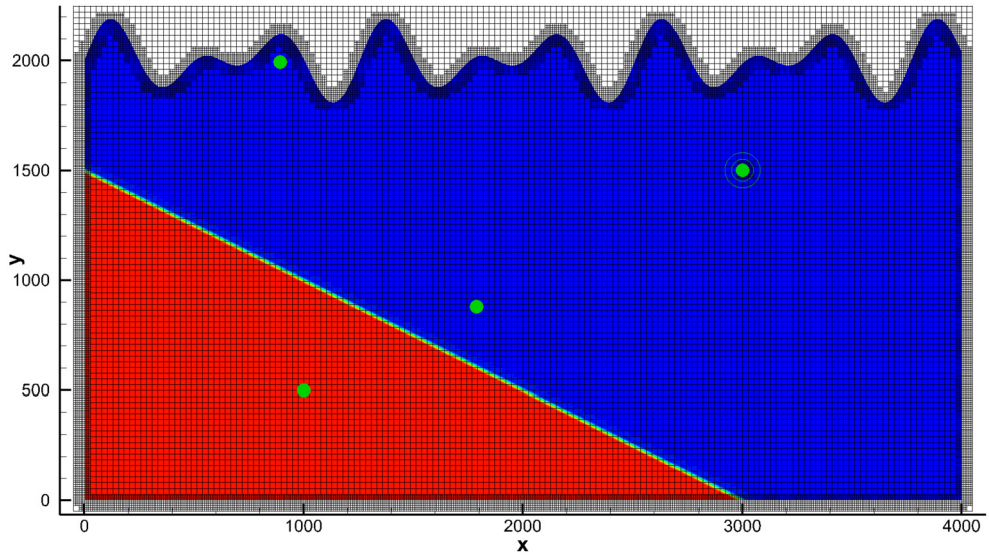

Fig. 10. Wave propagation in complex 2D geometry. Computational domain and AMR grid for the diffuse interface approach, colored by the mass density.

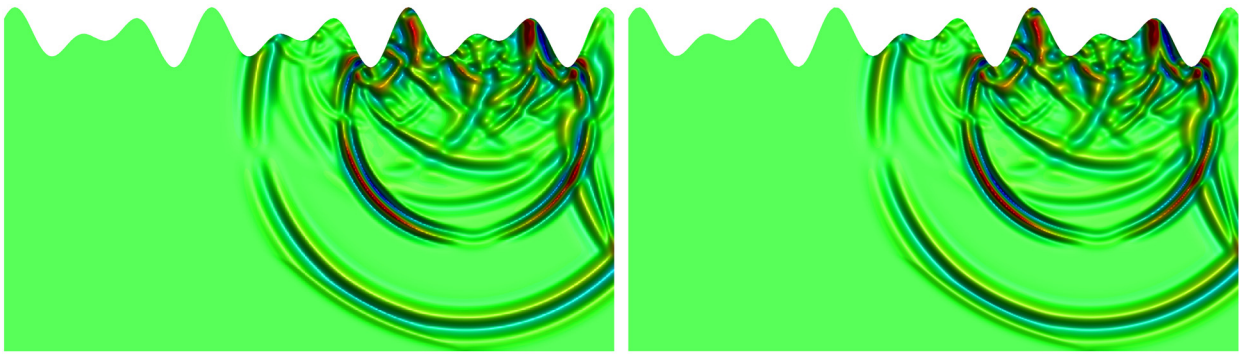

Fig. 11. Wave propagation in complex 2D geometry. Comparison between the numerical solution obtained with the diffuse interface approach (left) and the reference solution (right) for σ_{xx} at $t = 0.5$. For the diffuse interface results, only the physically relevant part of the domain is shown.

Table 4
p- and s-wave speeds in the two layers used for the wave propagation problem in complex geometry.

Zone	c_p (m/s)	c_s (m/s)	Location
1	3200.00	1847.50	$y > 1500 - \frac{x}{2}$
2	2262.74	1306.38	$y \leq 1500 - \frac{x}{2}$

Table 5
Receiver locations used for the seismogram recordings in the wave propagation problem in complex geometry.

Receiver	1	2	3
x	893.80	1790.0	1000.0
y	1994.83	880.0	500.0

to the one presented on the community website *sismowine*.[1] The heterogeneous material consists in two layers, whose parameters are specified in Table 6.

[1] The reference solution and the computational setup are available at http://www.sismowine.org/home.html, for the detailed description see http://www.sismowine.org/model/WP2_LOH1.pdf (sismowine.LOH.1).

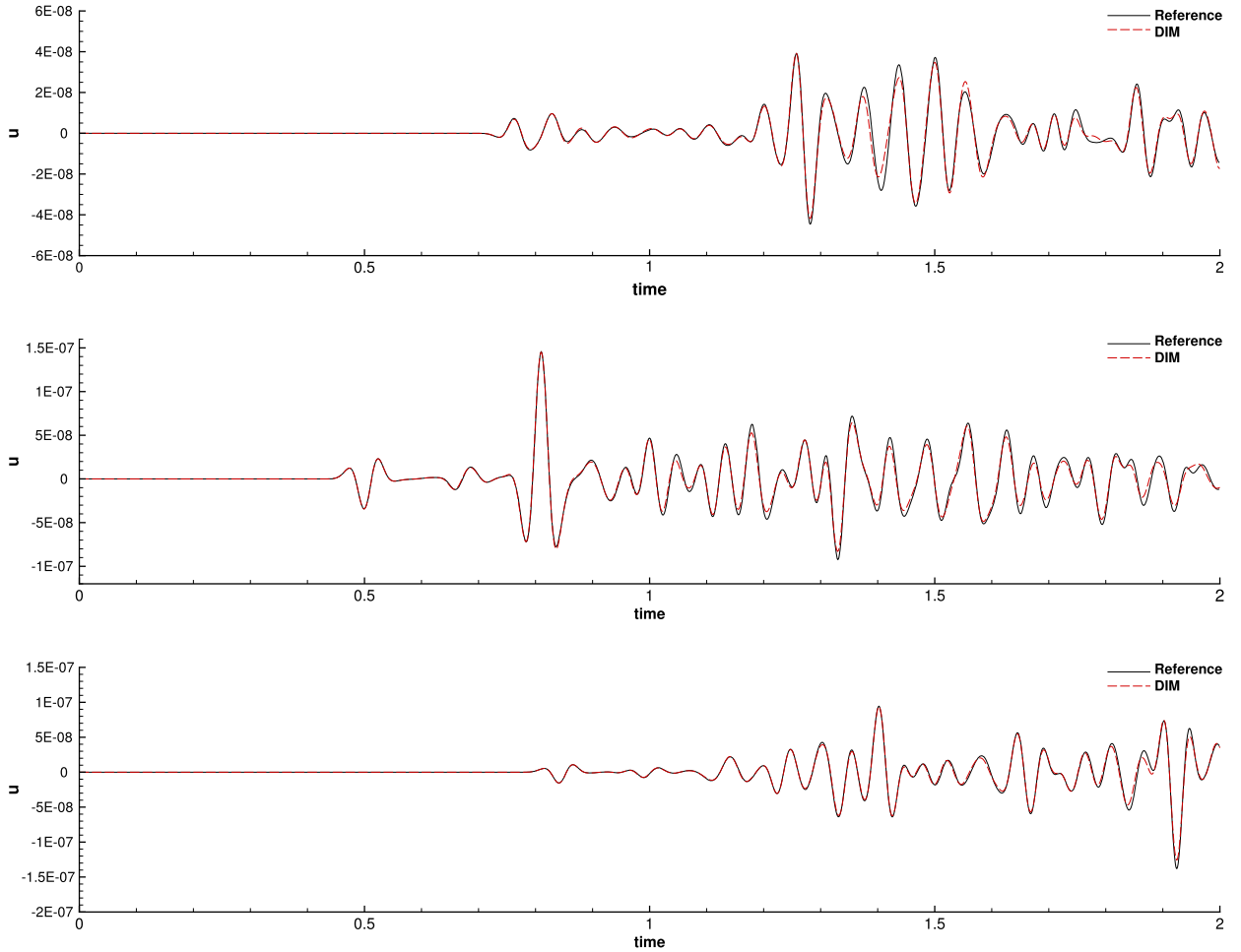

Fig. 12. Wave propagation in complex 2D geometry. Comparison of the velocity component u at the three receivers $1-3$ from top to bottom.

In our version of the LOH.1 benchmark we use a domain $\Omega = [-10750\text{ m}, 9250\text{ m}]^2 \times [-7000\text{ m}, 1000\text{ m}]$ covered with a uniform Cartesian grid of $80 \times 80 \times 64$ elements, which corresponds to a mesh spacing of $\Delta x = \Delta y = 250$ m and $\Delta z = 125$ m. Note that in our setup the computational domain Ω also extends above $z > 0$ and the free surface boundary condition in $z = 0$ is merely imposed by setting a jump in the solid volume fraction α, i.e. we set $\alpha = 1$ for all $z \leq 0$ and $\alpha = 0$ if $z > 0$. Close to the free surface in $z = 0$ we activate one additional level of adaptive mesh refinement with a refinement factor of $\mathfrak{r} = 3$. The wave propagation is driven by a point source placed two kilometers below the free surface in $\mathbf{x}_s = (0\text{ m}, 0\text{ m}, -2000\text{ m})$. The point source introduces a non-zero entry only on the seismic moment tensor components $M_{xy} = M_{yx} = M_0$. The used moment-rate history is given by

$$S^T(t) = M_0 \frac{t}{T^2} e^{\frac{-t}{T}}, \tag{46}$$

where $T = 0.1$ s and $M_0 = 10^{18}$ Nm. As suggested in the original report [122] and [35], the raw data from the time series is deconvolved and replaced with a Gaussian of spread 0.05. Figs. 17 and 18 show the time history recorded in two stations corresponding to station 8 and 9 of the document published in the community website *sismowine.LOH.1*. For each station we compute also the relative seismogram misfit, defined as

$$E = \frac{\sum_{j=1}^{n_t} \left(s_j - s_j^a\right)^2}{\sum_{j=1}^{n_t} \left(s_j^a\right)^2}, \tag{47}$$

where n_t indicates the number of samples; s_j and s_j^a are respectively the numerical and analytical value of the observed quantity at time t^j. The resulting errors are reported in Table 7 for all the three receivers and for all the velocity components.

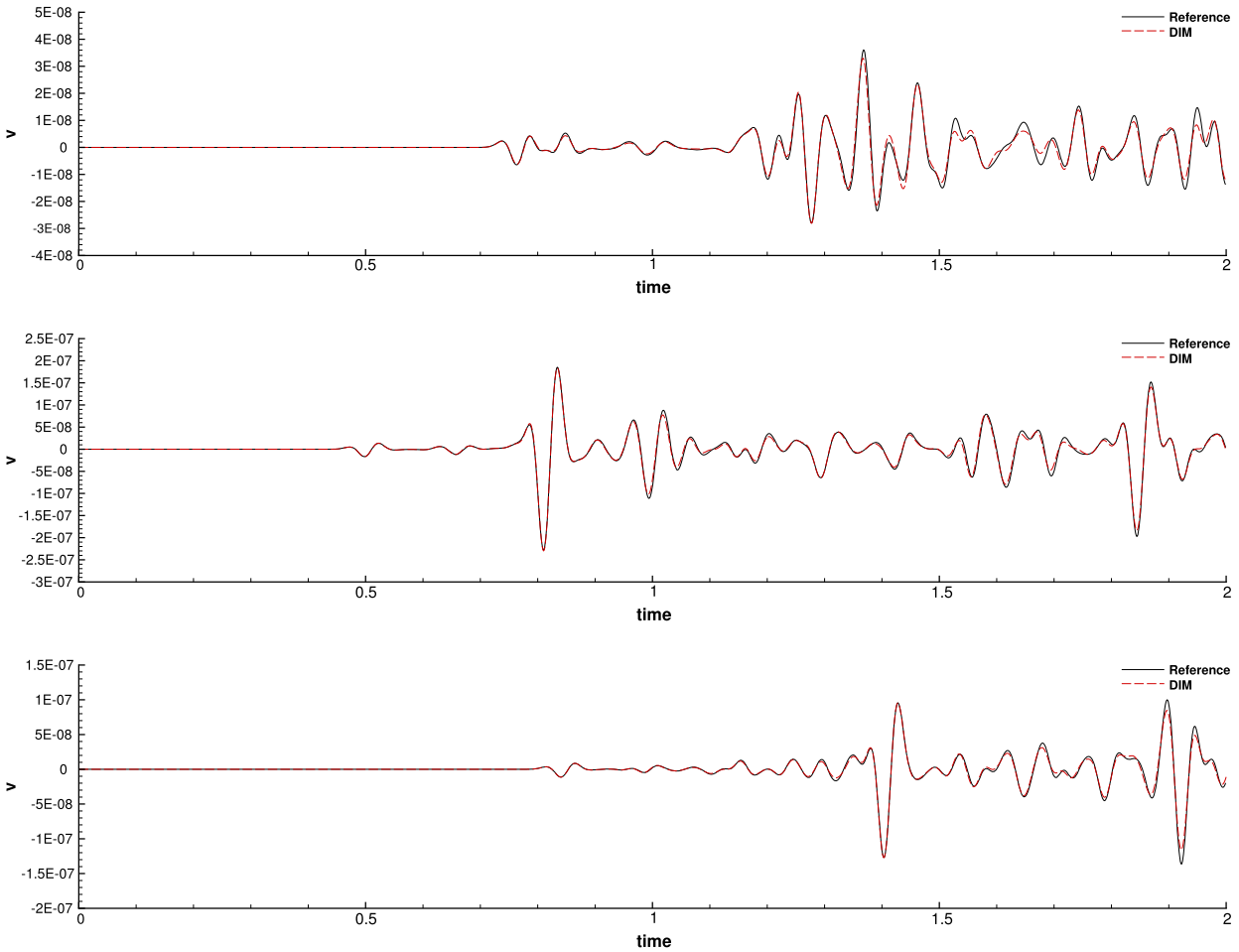

Fig. 13. Wave propagation in complex 2D geometry. Comparison of the velocity component v at the three receivers $1-3$ from top to bottom.

We obtain a good match between numerical and analytical solution, confirmed also by the values of the seismic misfit E. In Station 7, which is placed at 693 m from the epicenter, we register a very good matching with the analytical solution. This means, in particular, that the time signal of the point source is properly resolved. We note that point sources can be naturally implemented within the DG framework, since the spatial integral of the point source can always be evaluated analytically, thanks to the properties of the delta distribution, see [34,35].

The time signal captured in Station 9, which is 10.39 km from the epicenter, shows a higher error, but is still close to the results obtained in [35].

4.7. Wave propagation in a complex 3D geometry

We finally test the potential of our new diffuse interface approach for the simulation of more realistic applications. For this purpose we use a free surface topology based on the real DTM data of the Mont Blanc region.[2] The horizontal extent of the domain is 28 km in the x and y directions and ranges from 12 km below the sea level to 7 km above it in z direction. We use a heterogeneous material whose parameters are specified in Table 8. An initial velocity perturbation is placed in $\mathbf{x}_0 = (0, 0, 0)$ for the vertical component of the velocity

$$w(\mathbf{x}, 0) = ae^{-r^2/R^2}, \tag{48}$$

with $r = \|\mathbf{x}\|$, $a = -10^{-2}$ and $R = 300$ m. All other variables for the velocity and the stress tensor are set to zero. The computational domain is covered with a uniform Cartesian grid of $80 \times 80 \times 80$ elements and one refinement level is adopted close to the free surface. In order to represent the complex surface topography within our diffuse interface approach, all

[2] The DTM data have been taken from http://geodati.fmach.it/gfoss_geodata/libro_gfoss/. Our computational domain is centered with respect to the UTM coordinates (340000.0, 5075000.0).

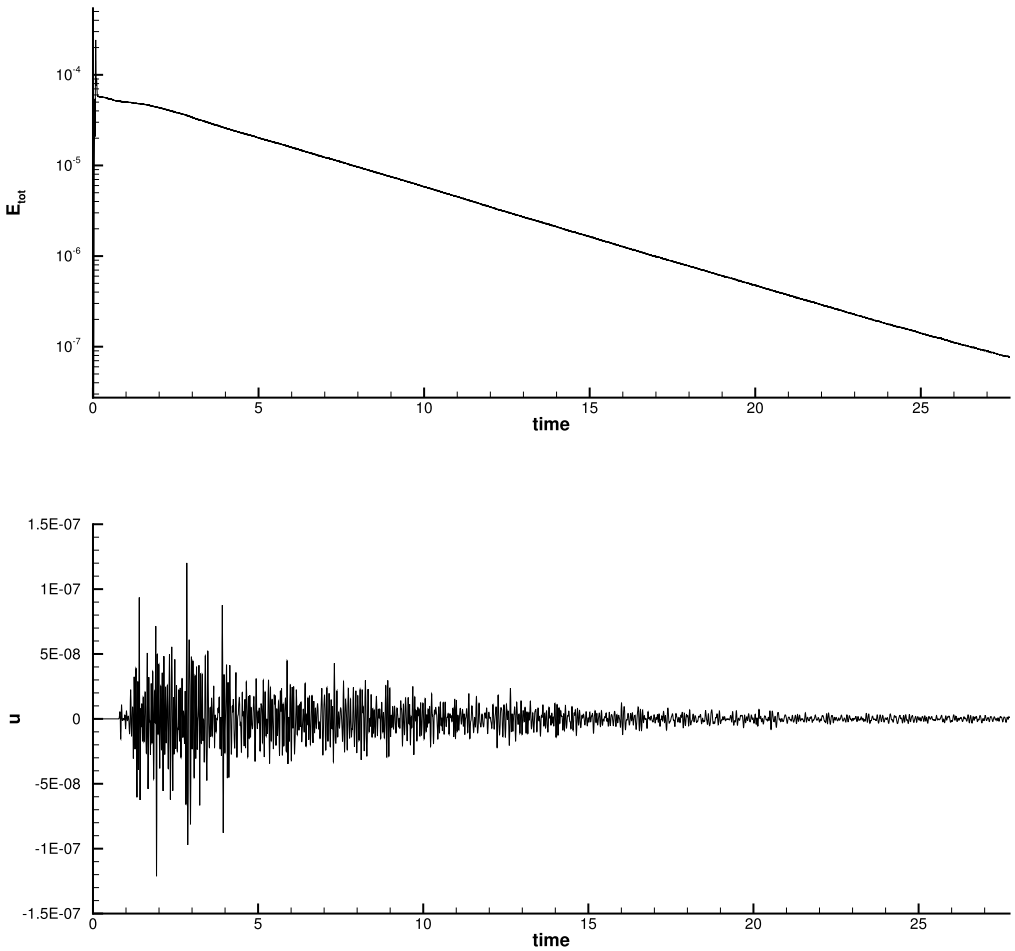

Fig. 14. Wave propagation in complex 2D geometry. Total energy decay (top) and long-time seismogram recording with decreasing amplitude (bottom). The proposed scheme is observed to be dissipative and thus energy-stable, also for long-time simulations.

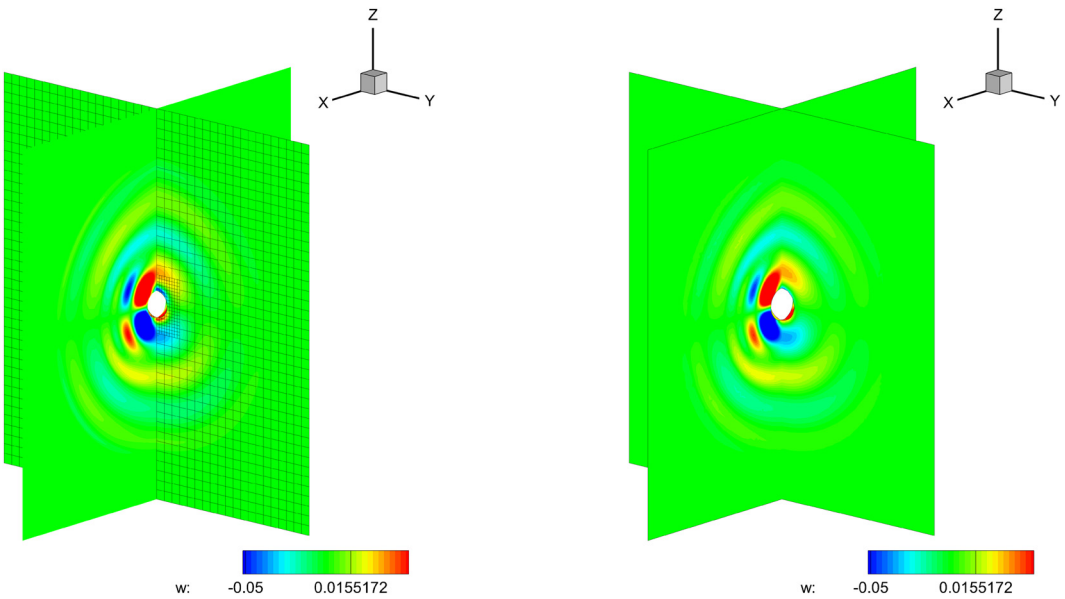

Fig. 15. Scattering of a plane wave on a sphere. Velocity component w at $t_{end} = 1.0$ obtained with the new diffuse interface method on AMR grid (left) and the unstructured reference code `SeisSol` (right).

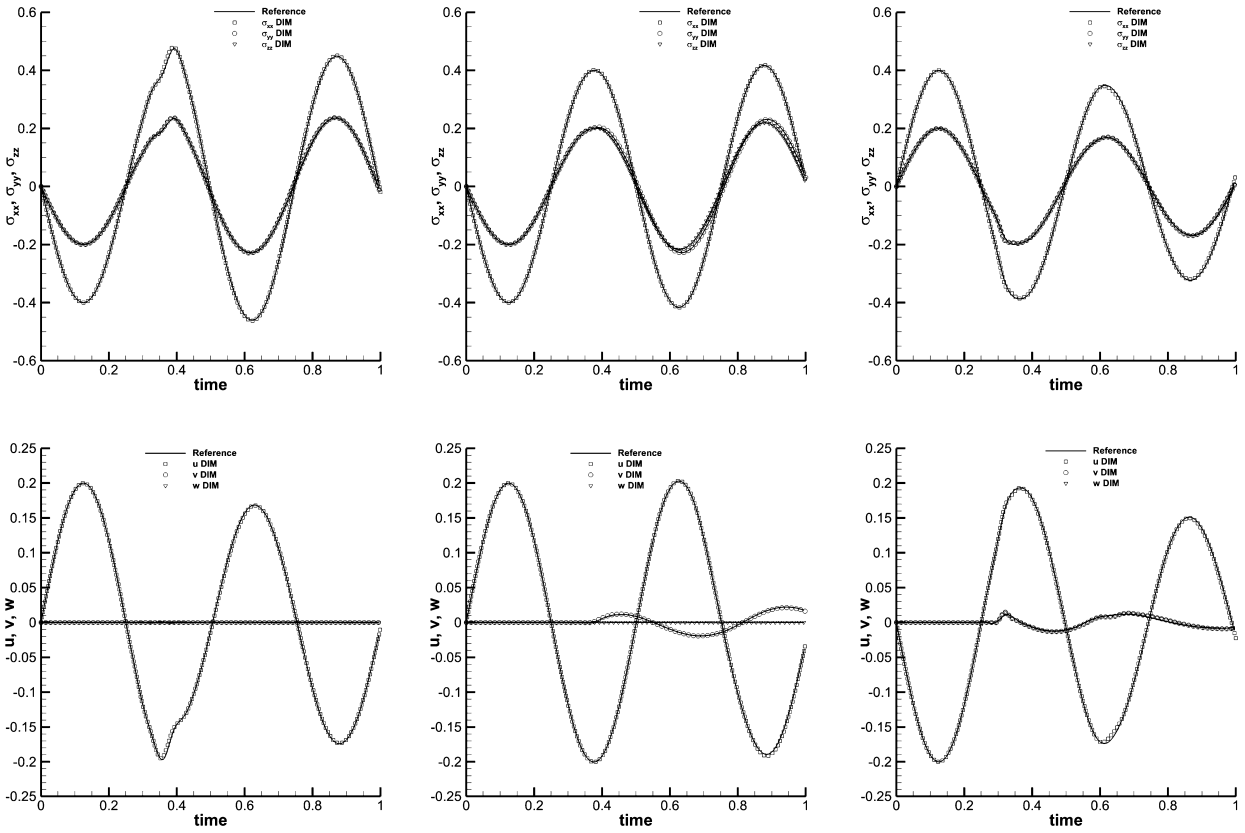

Fig. 16. Scattering of a plane wave on a sphere. Comparison of the resulting signal in the three receivers. In the first row we report the time series of the stress tensor components σ_{xx}, σ_{yy} and σ_{zz} for the receivers $1, 2, 3$, respectively, from left to right. In the second row the velocity signal is reported for the same receivers.

Table 6
Material parameters for the LOH.1 test case.

	Position	$c_p(\mathrm{m\,s^{-1}})$	$c_s(\mathrm{m\,s^{-1}})$	$\rho(\mathrm{kg\,m^{-3}})$	λ(GPa)	μ(GPa)
Medium 1	$z > -1000$ m	4000	2000	2600	20.8	10.4
Medium 2	$z \leq -1000$ m	6000	3464	2700	32.4	32.4

that is needed is to compute the shortest distance of a point $\mathbf{x}$ to the free surface defined by the DTM data in order to set the volume fraction function α according to (28) and (27). The DTM model is given on a Cartesian raster with a spatial resolution of 250 m, which we can then interpolate to any point in our computational domain through bilinear interpolation. The smoothing parameter for the diffuse interface zone is set to $I_D = 50$ m. The simulation with the diffuse interface method is run on the AMR grid with an ADER-DG scheme based on piecewise polinomials of degree $N = 3$ in space and time. In Fig. 19 we show a plot of the chosen Cartesian AMR grid with the free surface determined by α.

The reference solution is computed with an unstructured ADER-DG scheme [35] as used in the `SeisSol` code using $N_e = 1,267,717$ boundary-fitted tetrahedral elements and a polynomial approximation degree of $N = 3$ in space and time. A comparison of the numerical solution obtained with the new diffuse interface approach on adaptive Cartesian grids and the results obtained with the unstructured reference code is shown via contour surface maps in Fig. 20 at time $t = 2.0$. Overall, we can note a very good agreement between the two results. We also consider the time signals captured in four receivers, whose positions are reported in Table 9. They record data close to the free surface at 1 km, 5 km and 10 km distance from $\mathbf{x}_0$ (receivers $1 \ldots 3$) and at 3 km below the sea level with a distance of 5 km from $\mathbf{x}_0$ (receiver 4). The resulting time history of the velocity signals recorded by the four receivers is reported in Fig. 21. A very good agreement between the new diffuse interface approach and the reference scheme can be observed also in this case with complex 3D geometry. Finally, in Fig. 22 we show the interpolation of the velocity component w at the free surface at two different times, where one can again observe a very good agreement between the numerical results obtained with the new diffuse interface method and the reference solution obtained on the boundary-fitted unstructured mesh.

It has to be pointed out that the setup of this test problem with the new diffuse interface approach is *completely automatic*, without requiring *any* manual user interaction. The entire setup process of the computational model starts with

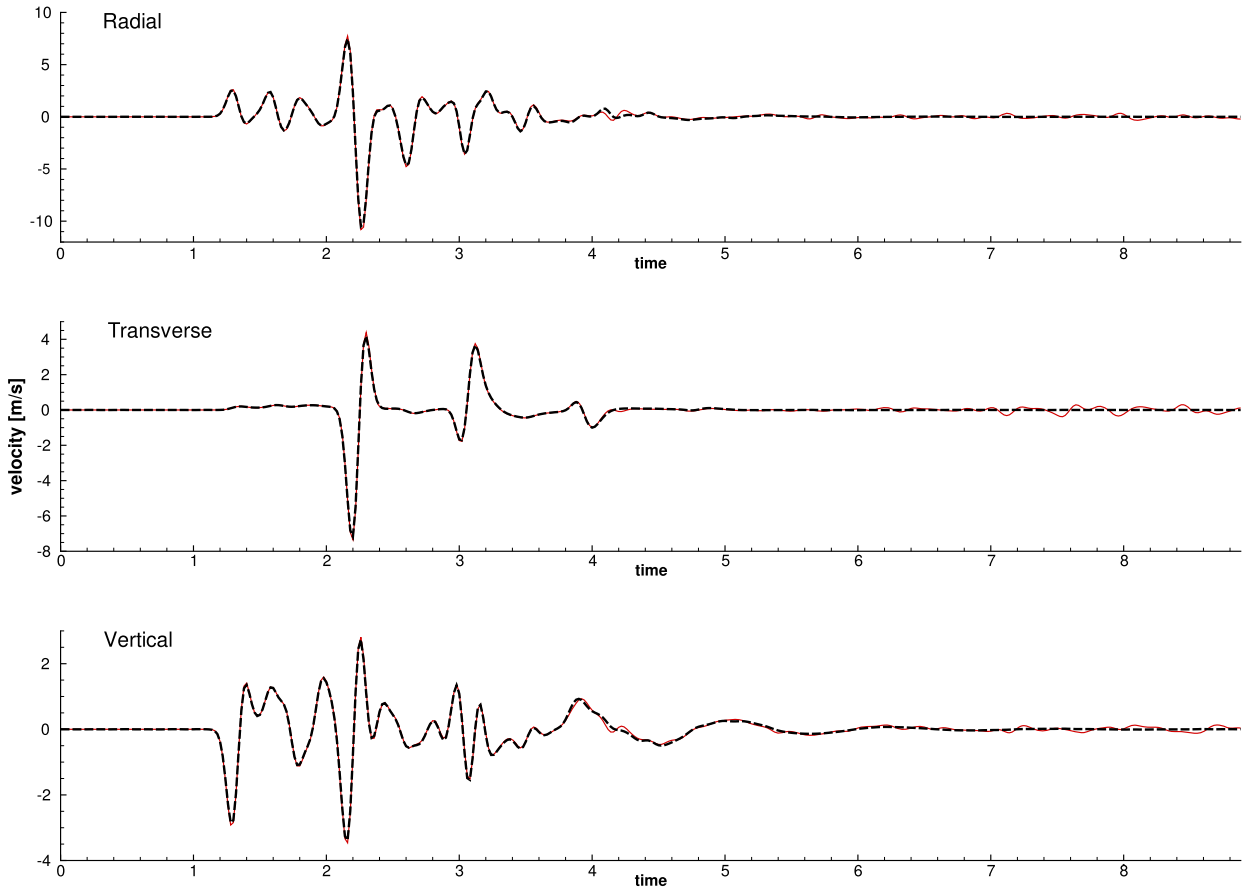

Fig. 17. Comparison of the radial, transverse and vertical velocity component for the LOH.1 test case on station 8. The exact solution (dashed black line) is compared against the numerical one (thin red line).

Table 7
Relative seismogram misfit E defined in Eq. (47) for the seismograms recorded in stations $7-9$ for the radial, transverse and vertical velocity component.

	E_{rad}	E_{trans}	E_{vert}
Station 7	0.000290	0.000555	0.000680
Station 8	0.004527	0.001788	0.003374
Station 9	0.074911	0.025004	0.027924

Table 8
Material parameters for the wave propagation test in a complex 3D geometry.

	Position	$c_p(\mathrm{m\,s^{-1}})$	$c_s(\mathrm{m\,s^{-1}})$	$\rho(\mathrm{kg\,m^{-3}})$	λ(GPa)	μ(GPa)
Medium 1	$z > -1000$ m	4000	2000	2600	20.8	10.4
Medium 2	$z \leq -1000$ m	6000	3464	2700	32.4	32.4

reading the DTM data from a file according to well-established standard GIS file formats, continues by automatically setting the color function α according to (28) and (27) with appropriate bilinear interpolation of the DTM data to the nodal degrees of freedom of the ADER-DG scheme and to the subcell FV averages and closes with the automatic setup of the adaptive Cartesian AMR grid based on the gradient of α up to the desired level of spatial resolution. We would like to emphasize again that for the diffuse interface approach the time step size does *not* depend on the distribution of α. In contrast to this fully automated chain in `ExaHyPE`, the setup of the same test case in `SeisSol` still requires the generation of a boundary-aligned unstructured tetrahedral mesh with an external grid generation tool that needs some manual interactions with the end user. For very complex surface topography, even more user interaction is required to obtain a high quality grid, which is essential due to the CFL restriction on the time step.

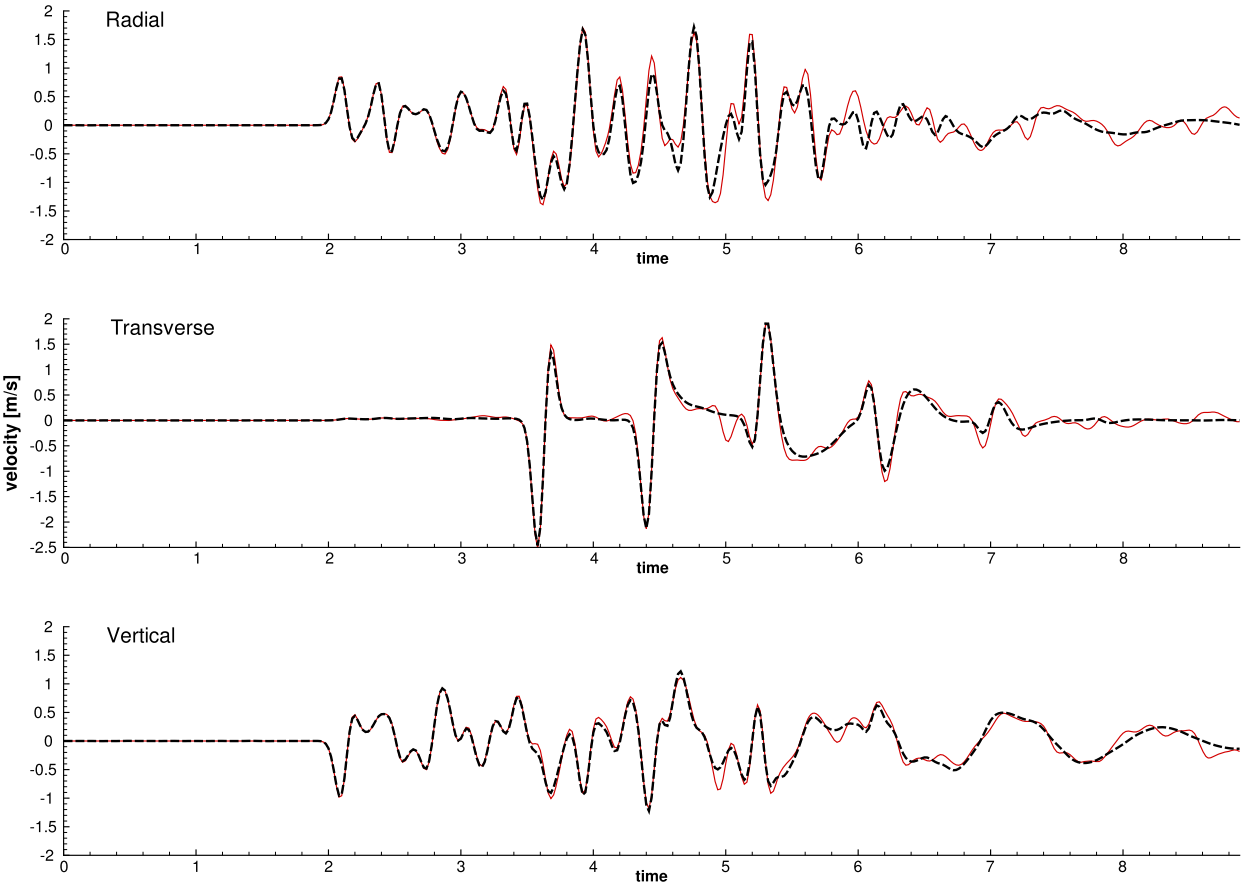

Fig. 18. Comparison of the radial, transverse and vertical velocity component for the LOH.1 test case on station 9. The exact solution (dashed black line) is compared against the numerical one (thin red line).

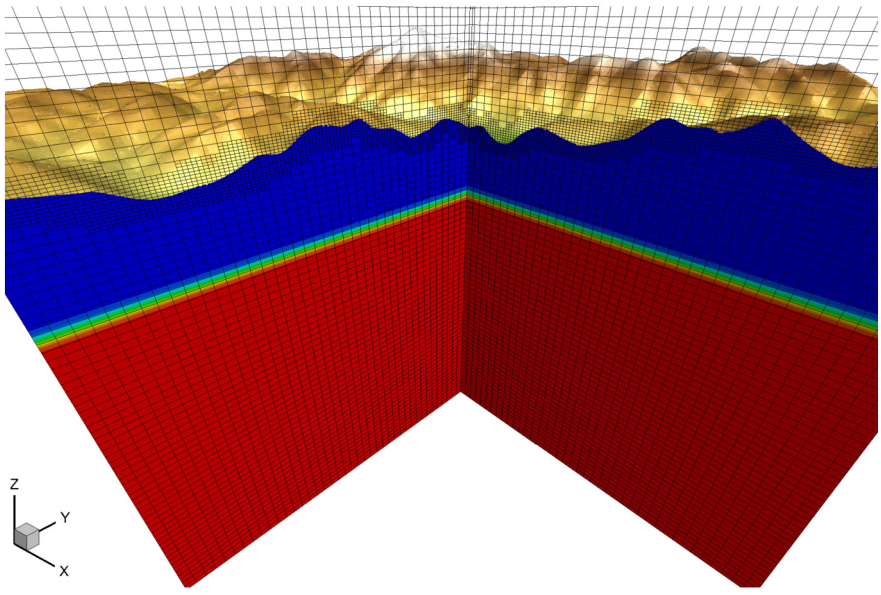

Fig. 19. Wave propagation in a realistic 3D geometry. Plot of the adaptive Cartesian mesh used for the test colored with the Lamé constant λ.

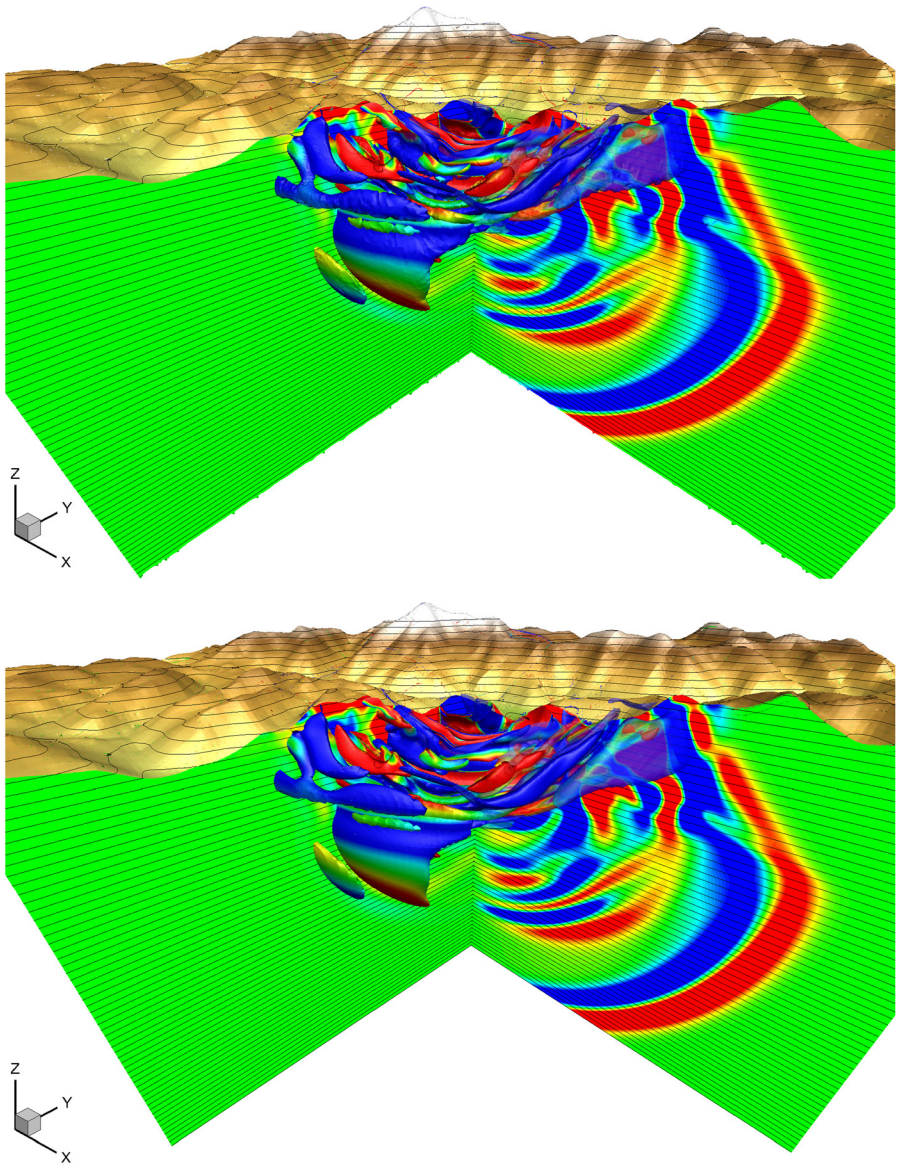

Fig. 20. Wave propagation in complex 3D geometry. Comparison of the ADER-DG reference solution on unstructured boundary-fitted grids (left) with the numerical solution obtained with the new diffuse interface method (DIM) on a Cartesian AMR mesh (right) at time $t = 2.0$. We show the iso-surfaces $\pm 4 \cdot 10^{-5}$ for the velocity components u and v colored by w. The slices are colored using the velocity component u.

Table 9
Receiver positions for the wave propagation test in complex 3D geometry.

Receiver	x	y	z
1	1000.000000	0.000000	1397.723250
2	3535.533906	3535.533906	1883.989778
3	8660.254038	5000.000000	2173.363299
4	1545.084972	4755.282581	-3000.000000

5. Conclusions

In this paper a novel diffuse interface method (DIM) for the simulation of seismic wave propagation in linear isotropic material with complex and even moving free surface topography has been proposed. The governing PDE system can be derived from a Baer-Nunziato-type model of compressible multi-phase flows [69–71,73] following similar ideas as those employed in [97–99]. In alternative, our governing equations can also be derived by combining the equations of nonlinear

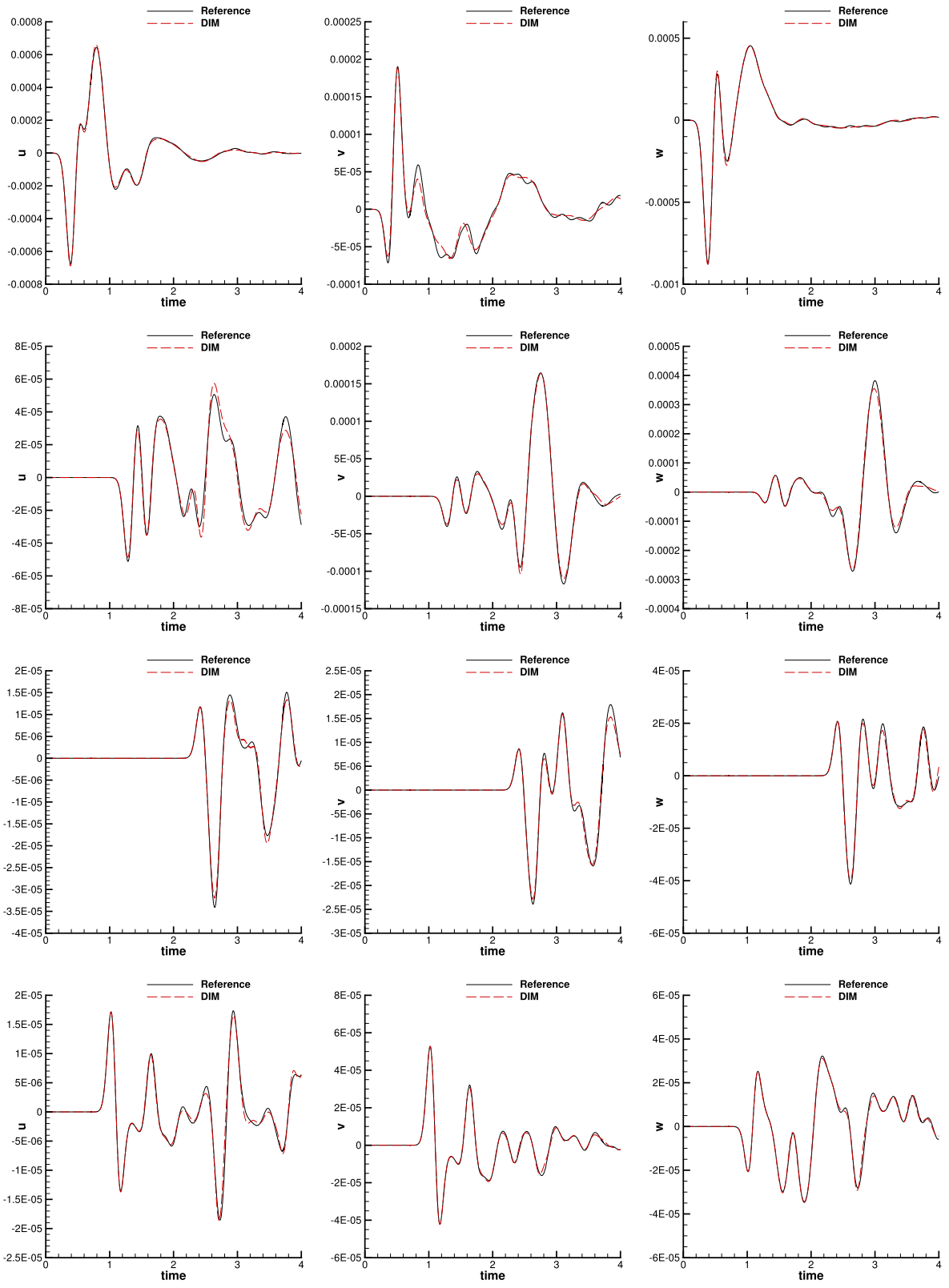

Fig. 21. Wave propagation in complex 3D geometry. Comparison of the time signal of the velocity field obtained with the new diffuse interface approach and the reference solution for the receiver 1 to 4 respectively from the top to the bottom row.

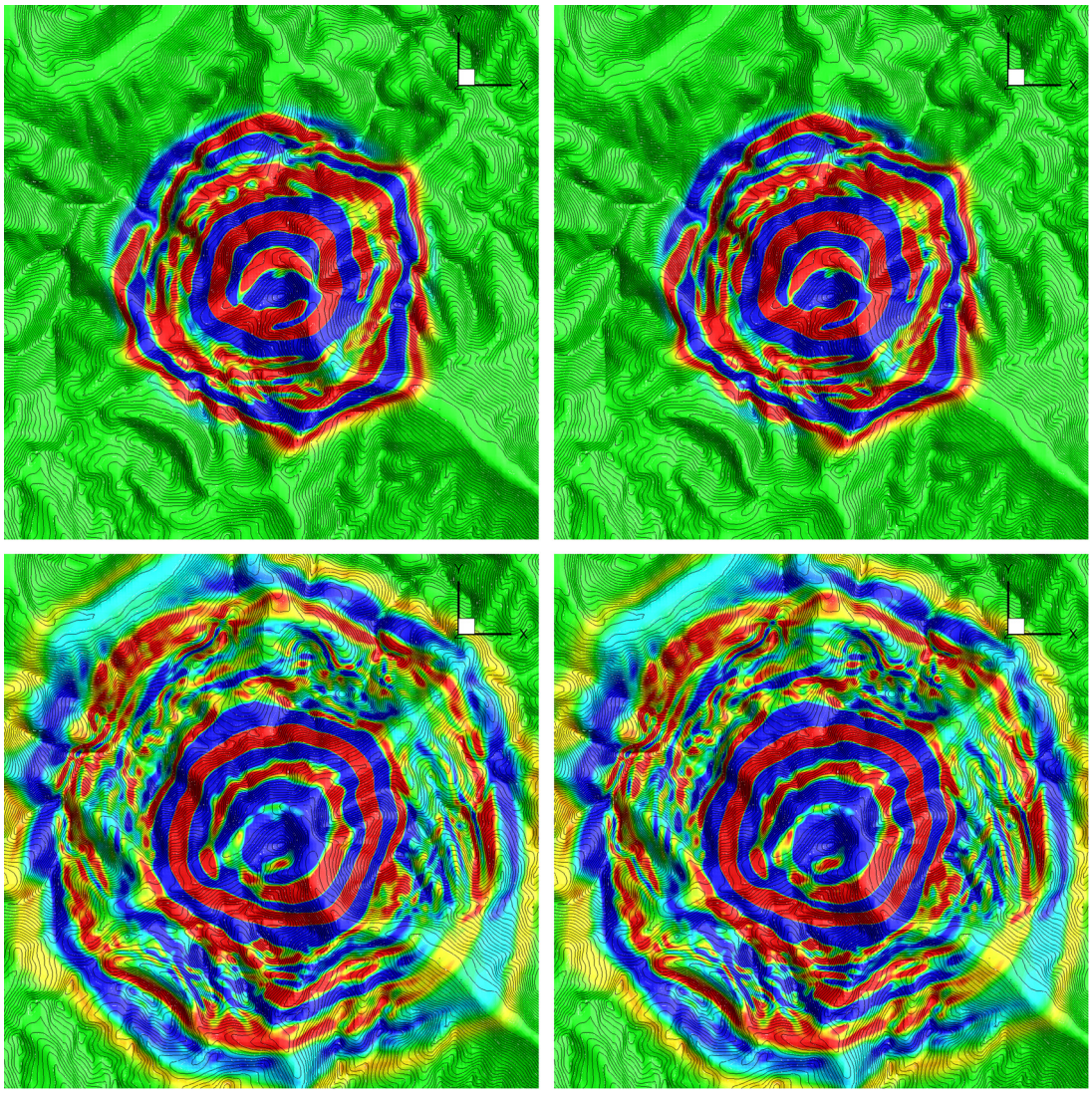

Fig. 22. Wave propagation in complex 3D geometry. Comparison of the interpolation of the vertical velocity w on the surface computed as the iso-surface $\alpha = 0.95$ between the diffuse interface approach (left) and the reference one (right) at time $t = 2.0$ and $t = 3.0$.

hyperelasticity in Eulerian coordinates of Godunov and Romenski [74,94,100] with the compressible multi-phase flow model of Romenski et al. [75,101].

In both cases, the velocity of the medium is supposed to be very small, so that the nonlinear convective terms can be neglected, and a linear material behavior according to Hooke's law is assumed. We have proven that the solution of the Riemann problem with arbitrary data and a jump of the volume fraction function α from one to zero yields a Godunov state at the interface in which the normal components of the stress tensor vanish, which is exactly the required free surface boundary condition $\boldsymbol{\sigma} \cdot \mathbf{n} = 0$. The free surface boundary condition on a physical domain Ω_p of arbitrary shape can therefore be properly imposed by defining a spatially variable scalar function α in the computational domain Ω, which has to be large enough to contain Ω_p, i.e. $\Omega_p \subset \Omega$, simply by setting $\alpha = 1$ for $\mathbf{x} \in \Omega_p$ and $\alpha = 0$ for $\mathbf{x} \notin \Omega_p$, without having to fit the boundary of the computational domain $\partial\Omega$ to the real boundary $\partial\Omega_p$ of the physical domain to be discretized. In practical simulations, the interface layer that contains the transition from $\alpha = 1$ to $\alpha = 0$ is slightly smoothed by a characteristic width I_D, which is the reason why we call our approach a diffuse interface method. We have carried out a systematic study in which we show that for vanishing interface thickness $I_D \to 0$ the correct wave reflection at the free surface boundary is obtained.

The governing equations derived in the first part of the paper have been solved on adaptive Cartesian meshes (AMR) via high order accurate ADER-DG schemes combined with a subcell finite volume limiter [88,87]. The use of the subcell finite volume limiter is necessary in regions with strong gradients of α in order to avoid spurious oscillations and unphysical solutions that would be obtained with a pure unlimited high order DG scheme. The practical implementation of the model

has been carried out in the ExaHyPE code developed within the European H2020 research project *An Exascale Hyperbolic PDE Engine*, see http://exahype.eu/. We have presented a large set of two- and three-dimensional wave propagation problems where we have compared the results obtained with the new diffuse interface approach with classical computational methods based on boundary-fitted unstructured meshes. In all cases under investigation, and even in the presence of complex surface topography, the new diffuse interface model performs very well as shown throughout this paper.

We stress again that the *key novelty* introduced here consists in the representation of the geometrically complex surface topography merely via the scalar solid volume fraction function α, instead of making use of complex structured or unstructured boundary-fitted meshes. In order to improve the spatial resolution of certain geometric features of the physical domain Ω_p, we simply use adaptive mesh refinement (AMR) on locally Cartesian grids. This allows a *fully automated workflow* in the setup of the computational model, without requiring any external mesh generation tools or any manual interaction with the user. We underline again that the time step restriction in our new approach is completely independent of the complexity of the geometry of the domain Ω_p to be discretized, since α has no influence on the eigenvalues of the governing PDE system. The admissible local time step size according to the CFL condition is therefore only given by the local mesh size h, the pressure wave propagation speed c_p and the polynomial approximation degree N.

We emphasize again that the use of a time-accurate local time stepping strategy (LTS) is crucial in order to avoid the reduction of the time step size Δt in regions that are far away from the diffuse interface and which can run the high order unlimited ADER-DG scheme on a coarse mesh.

Current work in progress is the implementation of new strategies for highly efficient small matrix-matrix multiplications in ADER-DG schemes on adaptive Cartesian grids (exploiting also the fact that we use a nodal tensor-product basis) in order to improve computational performance of the code, similar to the hardware optimizations already successfully applied in the context of the unstructured ADER-DG schemes used in SeisSol [120,121].

Future research will concern the extension of our new diffuse interface approach to the full equations of nonlinear hyperelasticity including large strains, moving solids, plastic deformations and dynamic rupture processes governed by nonlinear material rheologies. The mathematical model will be based on the Godunov-Peshkov-Romenski model presented and discussed in [74,94,100,76–79].

Acknowledgements

This research was funded by the European Union's Horizon 2020 Research and Innovation Programme under the project *ExaHyPE*, grant no. 671698 (call FETHPC-1-2014). The 3D simulations were performed on the HazelHen supercomputer at the HLRS in Stuttgart, Germany and on the SuperMUC supercomputer at the LRZ in Garching, Germany. The first two authors acknowledge funding from the Italian Ministry of Education, University and Research (MIUR) in the frame of the Departments of Excellence Initiative 2018–2022 (grant L. 232/2016), attributed to DICAM of the University of Trento. MD has also received support from the University of Trento in the frame of the Strategic Initiative *Modeling and Simulation*. The authors are also very grateful for the constructive comments and remarks of the Associate Editor and of the four anonymous referees, which helped to substantially improve the quality and readability of this paper.

References

[1] R. Madariaga, Dynamics of an expanding circular fault, Bull. Seismol. Soc. Am. 66 (1976) 639–666.
[2] J. Virieux, Sh-wave propagation in heterogeneous media: velocity–stress finite–difference method, Geophysics 49 (1984) 1933–1942.
[3] J. Virieux, P-sv wave propagation in heterogeneous media: velocity–stress finite–difference method, Geophysics 51 (1986) 889–901.
[4] A. Levander, Fourth-order finite difference p-sv seismograms, Geophysics 53 (1988) 1425–1436.
[5] P. Mora, Modeling anisotropic seismic waves in 3-d, SEG Society of Exploration Geophysicists, 1989, pp. 1039–1043.
[6] P. Moczo, J. Kristek, V. Vavrycuk, R. Archuleta, L. Halada, 3D heterogeneous staggered-grid finite-difference modeling of seismic motion with volume harmonic and arithmetic averaging of elastic moduli and densities, Bull. Seismol. Soc. Am. 92 (2002) 3042–3066.
[7] H. Igel, P. Mora, B. Riollet, Anisotropic wave propagation through finite-difference grids, Geophysics 60 (1995) 1203–1216.
[8] E. Tessmer, 3-d seismic modelling of general material anisotropy in the presence of the free surface by a chebyshev spectral method, Geophys. J. Int. 121 (1995) 557–575.
[9] S. Magnier, P. Mora, Finite differences on minimal grids, Geophysics 59 (1994) 1435–1443.
[10] M. Käser, H. Igel, Numerical simulation of 2d wave propagation on unstructured grids using explicit differential operators, Geophys. Prospect. 49 (2001) 607–619.
[11] M. Käser, H. Igel, A comparative study of explicit differential operators on arbitrary grids, J. Comput. Acoust. 9 (2001) 1111–1125.
[12] Z. Wang, Spectral (finite) volume method for conservation laws on unstructured grids: basic formulation, J. Comput. Phys. 178 (2002) 210–251.
[13] Z. Wang, Y. Liu, Spectral (finite) volume method for conservation laws on unstructured grids II: extension to two-dimensional scalar equation, J. Comput. Phys. 179 (2002) 665–697.
[14] Z. Wang, Y. Liu, Spectral (finite) volume method for conservation laws on unstructured grids III: one-dimensional systems and partition optimization, J. Sci. Comput. 20 (2004) 137–157.
[15] Z. Wang, Y. Liu, Spectral (finite) volume method for conservation laws on unstructured grids IV: extension to two-dimensional systems, J. Comput. Phys. 194 (2004) 716–741.
[16] M. Tadi, Finite volume method for 2D elastic wave propagation, Bull. Seismol. Soc. Am. 94 (2004) 1500–1509.
[17] E. Dormy, A. Tarantola, Numerical simulation of elastic wave propagation using a finite volume method, J. Geophys. Res. 100 (1995) 2123–2133.
[18] M. Dumbser, M. Käser, Arbitrary high order finite volume schemes for seismic wave propagation on unstructured meshes in 2d and 3d, Geophys. J. Int. 171 (2007) 665–694.
[19] M. Kristeková, J. Kristek, P. Moczo, S. Day, Misfit criteria for quantitative comparison of seismograms, Bull. Seismol. Soc. Am. 96 (2006) 1836–1850.

[20] M. Kristeková, J. Kristek, P. Moczo, Time-frequency misfit and goodness-of-fit criteria for quantitative comparison of time signals, Geophys. J. Int. 178 (2009) 813–825.
[21] M. Käser, V. Hermann, J. de la Puente, Quantitative accuracy analysis of the discontinuous Galerkin method for seismic wave propagation, Geophys. J. Int. 173 (2008) 990–999.
[22] P. Moczo, J. Kristek, M. Galis, P. Pazak, On accuracy of the finite-difference and finite-element schemes with respect to P-wave to S-wave speed ratio, Geophys. J. Int. 182 (2010) 493–510.
[23] A.T. Patera, A spectral-element method for fluid dynamics: laminar flow in a channel expansion, J. Comput. Phys. 144 (1984) 45–58.
[24] E. Priolo, J. Carcione, G. Seriani, Numerical simulation of interface waves by high-order spectral modeling techniques, J. Comput. Phys. 144 (1984) 45–58.
[25] D. Komatitsch, J. Vilotte, The spectral-element method: an efficient tool to simulate the seismic response of 2d and 3d geological structures, Bull. Seismol. Soc. Am. 88 (1998) 368–392.
[26] G. Seriani, 3-d large-scale wave propagation modeling by a spectral-element method on a cray t3e multiprocessor, Comput. Methods Appl. Mech. Eng. 164 (1998) 235–247.
[27] D. Komatitsch, J. Tromp, Introduction to the spectral-element method for 3-d seismic wave propagation, Geophys. J. Int. 139 (1999) 806–822.
[28] D. Komatitsch, J. Tromp, Spectral-element simulations of global seismic wave propagation-i. Validation, Geophys. J. Int. 149 (2002) 390–412.
[29] E. Tessmer, D. Kosloff, 3-d elastic modelling with surface topography by a chebyshev spectral method, Geophysics 59 (1994) 464–473.
[30] H. Igel, Wave propagation in three-dimensional spherical sections by the chebyshev spectral method, Geophys. J. Int. 136 (1999) 559–566.
[31] G. Scovazzi, B. Carnes, Weak boundary conditions for wave propagation problems in confined domains: formulation and implementation using a variational multiscale method, Comput. Methods Appl. Mech. Eng. 221–222 (2012) 117–131.
[32] T. Song, G. Scovazzi, A Nitsche method for wave propagation problems in time domain, Comput. Methods Appl. Mech. Eng. 293 (2015) 481–521.
[33] G. Scovazzi, T. Song, X. Zeng, A velocity/stress mixed stabilized nodal finite element for elastodynamics: analysis and computations with strongly and weakly enforced boundary conditions, Comput. Methods Appl. Mech. Eng. 325 (2017) 532–576.
[34] M. Käser, M. Dumbser, An arbitrary high-order discontinuous Galerkin method for elastic waves on unstructured meshes - I. The two-dimensional isotropic case with external source terms, Geophys. J. Int. 166 (2006) 855–877.
[35] M. Dumbser, M. Käser, An arbitrary high-order discontinuous Galerkin method for elastic waves on unstructured meshes - II. The three-dimensional isotropic case, Geophys. J. Int. 167 (2006) 319–336.
[36] M. Dumbser, M. Käser, E.F. Toro, An arbitrary high–order Discontinuous Galerkin method for elastic waves on unstructured meshes - V. Local time stepping and p-adaptivity, Geophys. J. Int. 171 (2007) 695–717.
[37] M. Grote, A. Schneebeli, D. Schötzau, Discontinuous Galerkin finite element method for the wave equation, SIAM J. Numer. Anal. 44 (2006) 2408–2431.
[38] P. Antonietti, I. Mazzieri, A. Quarteroni, F. Rapetti, Non-conforming high order approximations of the elastodynamics equation, Comput. Methods Appl. Mech. Eng. 209–212 (2012) 212–238.
[39] P. Antonietti, C. Marcati, I. Mazzieri, A. Quarteroni, High order discontinuous Galerkin methods on simplicial elements for the elastodynamics equation, Numer. Algorithms 71 (2016) 181–206.
[40] J.J.W. van der Vegt, H. van der Ven, Space–time discontinuous Galerkin finite element method with dynamic grid motion for inviscid compressible flows I. General formulation, J. Comput. Phys. 182 (2002) 546–585.
[41] H. van der Ven, J.J.W. van der Vegt, Space–time discontinuous Galerkin finite element method with dynamic grid motion for inviscid compressible flows II. Efficient flux quadrature, Comput. Methods Appl. Mech. Eng. 191 (2002) 4747–4780.
[42] C. Klaij, J.J.W.V. der Vegt, H.V. der Ven, Space-time discontinuous Galerkin method for the compressible Navier-Stokes equations, J. Comput. Phys. 217 (2006) 589–611.
[43] S. Rhebergen, B. Cockburn, A space–time hybridizable discontinuous Galerkin method for incompressible flows on deforming domains, J. Comput. Phys. 231 (2012) 4185–4204.
[44] S. Rhebergen, B. Cockburn, J.J. van der Vegt, A space-time discontinuous Galerkin method for the incompressible Navier-Stokes equations, J. Comput. Phys. 233 (2013) 339–358.
[45] M. Balazsova, M. Feistauer, On the stability of the ALE space-time discontinuous Galerkin method for nonlinear convection-diffusion problems in time-dependent domains, Appl. Math. 60 (2015) 501–526.
[46] M. Balazsova, M. Feistauer, M. Hadrava, A. Kosik, On the stability of the space-time discontinuous Galerkin method for the numerical solution of nonstationary nonlinear convection-diffusion problems, J. Numer. Math. 23 (2015) 211–233.
[47] P. Antonietti, I. Mazzieri, A. Quarteroni, F. Rapetti, High order space-time discretization for elastic wave propagation problems, in: M. Azaiez, H.E. Fekihand, J. Hestaven (Eds.), Proceedings of ICOSAHOM 2012, in: Lect. Notes Comput. Sci. Eng., vol. 95, Springer Verlag, 2014, pp. 87–97.
[48] P. Antonietti, N.D. Santo, I. Mazzieri, A. Quarteroni, A high-order discontinuous Galerkin approximation to ordinary differential equations with applications to elastodynamics, IMA J. Numer. Anal. 38 (2018) 1709–1734.
[49] M. Tavelli, M. Dumbser, Arbitrary high order accurate space-time discontinuous Galerkin finite element schemes on staggered unstructured meshes for linear elasticity, J. Comput. Phys. 366 (2018) 386–414.
[50] M. Dumbser, V. Casulli, A staggered semi-implicit spectral discontinuous Galerkin scheme for the shallow water equations, Appl. Math. Comput. 219 (15) (2013) 8057–8077.
[51] M. Tavelli, M. Dumbser, A high order semi-implicit discontinuous Galerkin method for the two dimensional shallow water equations on staggered unstructured meshes, Appl. Math. Comput. 234 (2014) 623–644.
[52] M. Tavelli, M. Dumbser, A staggered arbitrary high order semi-implicit discontinuous Galerkin method for the two dimensional incompressible Navier-Stokes equations, Comput. Fluids 119 (2015) 235–249.
[53] M. Tavelli, M. Dumbser, A staggered, space-time discontinuous Galerkin method for the three-dimensional incompressible Navier-Stokes equations on unstructured tetrahedral meshes, J. Comput. Phys. 319 (2016) 294–323.
[54] F. Fambri, M. Dumbser, Spectral semi-implicit and space-time discontinuous Galerkin methods for the incompressible Navier-Stokes equations on staggered Cartesian grids, Appl. Numer. Math. 110 (2016) 41–74.
[55] M. Tavelli, M. Dumbser, A pressure–based semi–implicit space–time discontinuous Galerkin method on staggered unstructured meshes for the solution of the compressible Navier–Stokes equations at all Mach numbers, J. Comput. Phys. 341 (2017) 341–376.
[56] F. Fambri, M. Dumbser, Semi-implicit discontinuous Galerkin methods for the incompressible Navier–Stokes equations on adaptive staggered Cartesian grids, Comput. Methods Appl. Mech. Eng. 324 (2017) 170–203.
[57] M. Bern, D. Eppstein, Mesh generation and optimal triangulation, in: Computing in Euclidean Geometry, vol. 1, 1992, pp. 23–90.
[58] B. Joe, Construction of three-dimensional improved-quality triangulations using local transformations, SIAM J. Sci. Comput. 16 (1995) 1292–1307.
[59] P. Fleischmann, W. Pyka, S. Selberherr, Mesh generation for application in technology cad, IEICE Trans. Electron. 82 (C) (1999) 937–947.
[60] S.W. Cheng, T.K. Dey, H. Edelsbrunner, M.A. Facello, S.H. Teng, Sliver exudation, J. ACM 47 (2000) 883–904.
[61] H. Edelsbrunner, D. Guoy, An experimental study of sliver exudation, Eng. Comput. 18 (2002) 229–240.
[62] A. Taube, M. Dumbser, C. Munz, R. Schneider, A high order discontinuous Galerkin method with local time stepping for the Maxwell equations, Int. J. Numer. Model. 22 (2009) 77–103.

[63] M. Grote, T. Mitkova, High-order explicit local time-stepping methods for damped wave equations, J. Comput. Appl. Math. 239 (2013) 270–289.
[64] M. Grote, T. Mitkova, Explicit local time-stepping methods for Maxwell's equations, J. Comput. Appl. Math. 234 (2010) 3283–3302.
[65] L. Gao, R. Brossier, B. Pajot, J. Tago, J. Virieux, An immersed free-surface boundary treatment for seismic wave simulation, Geophysics 80 (2015) T193–T209.
[66] B. Lombard, J. Piraux, C. Gélis, J. Virieux, Free and smooth boundaries in 2-D finite-difference schemes for transient elastic waves, Geophys. J. Int. 172 (2008) 252–261.
[67] W. Hu, An improved immersed boundary finite-difference method for seismic wave propagation modeling with arbitrary surface topography, Geophysics 81 (2016) T311–T322.
[68] B. Martin, B. Fornberg, Eismic modeling with radial basis function–generated finite differences (RBF–FD) – a simplified treatment of interfaces, J. Comput. Phys. 335 (2017) 828–845.
[69] M.R. Baer, J.W. Nunziato, A two-phase mixture theory for the deflagration-to-detonation transition (DDT) in reactive granular materials, Int. J. Multiph. Flow 12 (1986) 861–889.
[70] R. Saurel, R. Abgrall, A multiphase Godunov method for compressible multifluid and multiphase flows, J. Comput. Phys. 150 (1999) 425–467.
[71] R. Saurel, R. Abgrall, A simple method for compressible multifluid flows, SIAM J. Sci. Comput. 21 (1999) 1115–1145.
[72] R. Abgrall, B. Nkonga, R. Saurel, Efficient numerical approximation of compressible multi-material flow for unstructured meshes, Comput. Fluids 32 (2003) 571–605.
[73] R. Abgrall, R. Saurel, Discrete equations for physical and numerical compressible multiphase mixtures, J. Comput. Phys. 186 (2003) 361–396.
[74] S.K. Godunov, E.I. Romenski, Nonstationary equations of the nonlinear theory of elasticity in Euler coordinates, J. Appl. Mech. Tech. Phys. 13 (1972) 868–885.
[75] E. Romenski, Hyperbolic systems of thermodynamically compatible conservation laws in continuum mechanics, Math. Comput. Model. 28 (1998) 115–130.
[76] E.I. Romenskii, Deformation model for brittle materials and the structure of failure waves, J. Appl. Mech. Tech. Phys. 48 (3) (2007) 437–444.
[77] I. Peshkov, E. Romenski, A hyperbolic model for viscous Newtonian flows, Contin. Mech. Thermodyn. 28 (2016) 85–104.
[78] M. Dumbser, I. Peshkov, E. Romenski, O. Zanotti, High order ADER schemes for a unified first order hyperbolic formulation of continuum mechanics: viscous heat-conducting fluids and elastic solids, J. Comput. Phys. 314 (2016) 824–862.
[79] M. Dumbser, I. Peshkov, E. Romenski, O. Zanotti, High order ADER schemes for a unified first order hyperbolic formulation of Newtonian continuum mechanics coupled with electro-dynamics, J. Comput. Phys. 348 (2017) 298–342.
[80] E.I. Romenskii, E.B. Lys', V.A. Cheverda, M.I. Epov, Dynamics of deformation of an elastic medium with initial stresses, J. Appl. Mech. Tech. Phys. 58 (2017) 914–923.
[81] S. Ndanou, N. Favrie, S. Gavrilyuk, Multi-solid and multi-fluid diffuse interface model: applications to dynamic fracture and fragmentation, J. Comput. Phys. 295 (2015) 523–555.
[82] N. Favrie, S.L. Gavrilyuk, Diffuse interface model for compressible fluid-compressible elastic-plastic solid interaction, J. Comput. Phys. 231 (2012) 2695–2723.
[83] N. Favrie, S.L. Gavrilyuk, Solid-fluid diffuse interface model in cases of extreme deformations, J. Comput. Phys. 228 (2009) 6037–6077.
[84] S.L. Gavrilyuk, N. Favrie, R. Saurel, Modelling wave dynamics of compressible elastic materials, J. Comput. Phys. 227 (2008) 2941–2969.
[85] R. Saurel, F. Petitpas, R. Berry, Simple and efficient relaxation method for interfaces separating compressible fluids cavitating flows and shock in multiphase mixtures, J. Comput. Phys. 228 (2009) 1678–1712.
[86] A. Kapila, R. Menikoff, J. Bdzil, S. Son, D. Stewart, Two-phase modeling of ddt in granular materials: reduced equations, Phys. Fluids 13 (2001) 3002–3024.
[87] O. Zanotti, F. Fambri, M. Dumbser, A. Hidalgo, Space-time adaptive ADER discontinuous Galerkin finite element schemes with a posteriori subcell finite volume limiting, Comput. Fluids 118 (2015) 204–224.
[88] M. Dumbser, O. Zanotti, R. Loubère, S. Diot, A posteriori subcell limiting of the discontinuous Galerkin finite element method for hyperbolic conservation laws, J. Comput. Phys. 278 (2014) 47–75.
[89] S. Clain, S. Diot, R. Loubère, A high-order finite volume method for systems of conservation lawsmulti-dimensional optimal order detection (mood), J. Comput. Phys. 230 (2011) 4028–4050.
[90] S. Diot, S. Clain, R. Loubère, Improved detection criteria for the multi-dimensional optimal order detection (mood) on unstructured meshes with very high-order polynomials, Comput. Fluids 64 (2012) 43–63.
[91] M. Dumbser, D. Balsara, A new efficient formulation of the HLLEM Riemann solver for general conservative and non-conservative hyperbolic systems, J. Comput. Phys. 304 (2016) 275–319.
[92] M. Dumbser, D.S. Balsara, A new efficient formulation of the {HLLEM} riemann solver for general conservative and non-conservative hyperbolic systems, J. Comput. Phys. 304 (2016) 275–319.
[93] E.F. Toro, Riemann Solvers and Numerical Methods for Fluid Dynamics, 3rd edition, Springer, 2009.
[94] S.K. Godunov, E.I. Romenski, Elements of Continuum Mechanics and Conservation Laws, Kluwer Academic/ Plenum Publishers, 2003.
[95] A. Bedford, D. Drumheller, Elastic Wave Propagation, Wiley, Chichester, UK, 1994.
[96] A. Murrone, H. Guillard, A five equation reduced model for compressible two phase flow problems, J. Comput. Phys. 202 (2005) 664–698.
[97] M. Dumbser, A simple two–phase method for the simulation of complex free surface flows, Comput. Methods Appl. Mech. Eng. 200 (2011) 1204–1219.
[98] M. Dumbser, A diffuse interface method for complex three-dimensional free surface flows, Comput. Methods Appl. Mech. Eng. 257 (2013) 47–64.
[99] E. Gaburro, M. Castro, M. Dumbser, A well balanced diffuse interface method for complex nonhydrostatic free surface flows, Comput. Fluids 175 (2018) 180–198.
[100] S.K. Godunov, E.I. Romenski, Thermodynamics, conservation laws, and symmetric forms of differential equations in mechanics of continuous media, in: Computational Fluid Dynamics Review, vol. 95, John Wiley, NY, 1995, pp. 19–31.
[101] E. Romenski, D. Drikakis, E. Toro, Conservative models and numerical methods for compressible two-phase flow, J. Sci. Comput. 42 (2010) 68–95.
[102] M.J. Castro, J.M. Gallardo, C. Parés, High-order finite volume schemes based on reconstruction of states for solving hyperbolic systems with nonconservative products. Applications to shallow-water systems, Math. Comput. 75 (2006) 1103–1134.
[103] C. Parés, Numerical methods for nonconservative hyperbolic systems: a theoretical framework, SIAM J. Numer. Anal. 44 (2006) 300–321.
[104] M. Dumbser, E.F. Toro, A simple extension of the Osher Riemann solver to non-conservative hyperbolic systems, J. Sci. Comput. 48 (2011) 70–88.
[105] G.D. Maso, P.G. LeFloch, F. Murat, Definition and weak stability of nonconservative products, J. Math. Pures Appl. 74 (1995) 483–548.
[106] M. Dumbser, M. Castro, C. Parés, E. Toro, ADER schemes on unstructured meshes for non–conservative hyperbolic systems: applications to geophysical flows, Comput. Fluids 38 (2009) 1731–1748.
[107] M. Dumbser, A. Hidalgo, M. Castro, C. Parés, E.F. Toro, FORCE schemes on unstructured meshes II: non–conservative hyperbolic systems, Comput. Methods Appl. Mech. Eng. 199 (2010) 625–647.
[108] A. Harten, B. Engquist, S. Osher, S. Chakravarthy, Uniformly high order essentially non-oscillatory schemes, III, J. Comput. Phys. 71 (1987) 231–303.
[109] M. Dumbser, D.S. Balsara, E.F. Toro, C.D. Munz, A unified framework for the construction of one–step finite–volume and discontinuous Galerkin schemes, J. Comput. Phys. 227 (2008) 8209–8253.

[110] M. Dumbser, O. Zanotti, A. Hidalgo, D. Balsara, ADER-WENO finite volume schemes with space-time adaptive mesh refinement, J. Comput. Phys. 248 (2013) 257–286.
[111] H. Bungartz, M. Mehl, T. Neckel, T. Weinzierl, The PDE framework Peano applied to fluid dynamics: an efficient implementation of a parallel multiscale fluid dynamics solver on octree-like adaptive Cartesian grids, Comput. Mech. 46 (2010) 103–114.
[112] T. Weinzierl, M. Mehl, Peano-A traversal and storage scheme for octree-like adaptive Cartesian multiscale grids, SIAM J. Sci. Comput. 33 (2011) 2732–2760.
[113] A. Khokhlov, Fully threaded tree algorithms for adaptive refinement fluid dynamics simulations, J. Comput. Phys. 143 (2) (1998) 519–543.
[114] O. Zanotti, F. Fambri, M. Dumbser, A. Hidalgo, Space-time adaptive ADER discontinuous Galerkin finite element schemes with a posteriori subcell finite volume limiting, Comput. Fluids 118 (2015) 204–224.
[115] O. Zanotti, F. Fambri, M. Dumbser, Solving the relativistic magnetohydrodynamics equations with ADER discontinuous Galerkin methods, a posteriori subcell limiting and adaptive mesh refinement, Mon. Not. R. Astron. Soc. 452 (2015) 3010–3029.
[116] F. Fambri, M. Dumbser, O. Zanotti, Space-time adaptive ADER-DG schemes for dissipative flows: compressible Navier-Stokes and resistive MHD equations, Comput. Phys. Commun. 220 (2017) 297–318.
[117] M. Käser, M. Dumbser, A highly accurate discontinuous Galerkin method for complex interfaces between solids and moving fluids, Geophysics 73 (2008) T23–T35.
[118] M. Käser, M. Dumbser, An arbitrary high-order discontinuous Galerkin method for elastic waves on unstructured meshes - I. The two-dimensional isotropic case with external source terms, Geophys. J. Int. 166 (2006) 855–877.
[119] M. Dumbser, A. Hidalgo, O. Zanotti, High order space-time adaptive ADER-WENO finite volume schemes for non-conservative hyperbolic systems, Comput. Methods Appl. Mech. Eng. 268 (2014) 359–387.
[120] A. Breuer, A. Heinecke, M. Bader, C. Pelties, Accelerating SeisSol by generating vectorized code for sparse matrix operators, Adv. Parallel Comput. 25 (2014) 347–356.
[121] A. Breuer, A. Heinecke, S. Rettenberger, M. Bader, A. Gabriel, C. Pelties, Sustained petascale performance of seismic simulations with SeisSol on SuperMUC, Lect. Notes Comput. Sci. 8488 (2014) 1–18.
[122] S. Day, Tests of 3D elastodynamics codes, https://steveday.sdsu.edu/BASINS/Final_Report_1A01.pdf, 2001 (Accessed 25 October 2018).